RESEARCH ARTICLE

Key Points:
- Capacitive resistivity imaging (CRI) measures freezing and thawing in limestone
- Microseismic events with characteristics typical of cracking of rock bridges were detected during frost weathering experiments
- CRI and microseismic techniques offer a viable route for long-term monitoring of freeze-thaw and fracture in mountain rockwalls

Correspondence to:
J. B. Murton,
j.b.murton@sussex.ac.uk

Monitoring rock freezing and thawing by novel geoelectrical and acoustic techniques

Julian B. Murton[1], Oliver Kuras[2], Michael Krautblatter[3], Tim Cane[1], Dominique Tschofen[2], Sebastian Uhlemann[2,4], Sandra Schober[3], and Phil Watson[5,6]

[1]Permafrost Laboratory, Department of Geography, University of Sussex, Brighton, UK, [2]Geophysical Tomography, British Geological Survey, Nottingham, UK, [3]Landslide Research, Technische Universität München, Munich, Germany, [4]Institute of Geophysics, ETH Zurich, Zurich, Switzerland, [5]Sensor Technology Research Centre, Department of Engineering and Design, University of Sussex, Brighton, UK, [6]Apollo Fire Detectors Ltd, Havant, UK

Abstract Automated monitoring of freeze-thaw cycles and fracture propagation in mountain rockwalls is needed to provide early warning about rockfall hazards. Conventional geoelectrical methods such as electrical resistivity tomography (ERT) are limited by large and variable ohmic contact resistances, requiring galvanic coupling with metal electrodes inserted into holes drilled into rock, and which can be loosened by rock weathering. We report a novel experimental methodology that combined capacitive resistivity imaging (CRI), ERT, and microseismic event recording to monitor freeze-thaw of six blocks of hard and soft limestones under conditions simulating an active layer above permafrost and seasonally frozen rock in a nonpermafrost environment. Our results demonstrate that the CRI method is highly sensitive to freeze-thaw processes; it yields property information equivalent to that obtained with conventional ERT and offers a viable route for nongalvanic long-term geoelectrical monitoring, extending the benefits of the methodology to soft/hard rock environments. Contact impedances achieved with CRI are less affected by seasonal temperature changes, the aggregate state of the pore water (liquid or frozen), and the presence of low-porosity rock with high matrix resistivities than those achieved with ERT. Microseismic monitoring has the advantage over acoustic emissions that events were recorded in relevant field distances of meters to decameters from cracking events. For the first time we recorded about 1000 microcracking events and clustered them in four groups according to frequency and waveform. Compared to previous studies, mainly on ice-cracking in glaciers, the groups are attributed to single- or multiple-stage cracking events such as crack coalescence.

1. Introduction

Understanding the impacts of freezing and thawing on bedrock properties is fundamental to assessing the stability of mountain rockwalls. Remote monitoring of rockwall temperature and related geotechnical parameters is an emerging research field for geomorphology and geohazard mitigation. Geophysical tomography can contribute significantly to this field [*Harris et al.*, 2009] by characterizing volumetric properties of rock masses over time without the limitations of point sampling in boreholes. Both electrical and acoustic methods hold promise for long-term automated monitoring, but their systematic application to mountain permafrost is still rare, partly because sensor performance under repeated freeze-thaw conditions remains poorly understood. Although temperature-calibrated electrical resistivity tomography (ERT) with galvanic sensors can image movements of freezing fronts in rock [*Krautblatter and Hauck*, 2007; *Krautblatter et al.*, 2010], conventional geoelectrical methodology imposes practical limitations. The technique relies on galvanically coupled electrodes, which must be physically implanted into a substrate [*Loke et al.*, 2013]. For permafrost applications, this may lead to substantial magnitudes and variations in ohmic contact resistances between sensors and the host rock or soil as it freezes and thaws [*Krautblatter et al.*, 2010]. This introduces noise and can render individual sensors or indeed entire arrays unusable during the freezing periods, thus making quantitative interpretation of geoelectrical monitoring data challenging. Geoelectrical interpretation is complicated further where frost weathering leads to fracture and other changes in the physical properties of the rock. By contrast, strategic long-term thermal and geotechnical monitoring demands stable and predictable sensor properties and minimal bias of monitoring data due to the sensors themselves.

This paper reports a novel experimental design combining capacitively coupled resistivity sensors, conventional galvanic electrode arrays, and microseismic transducers to monitor noninvasively the dynamics
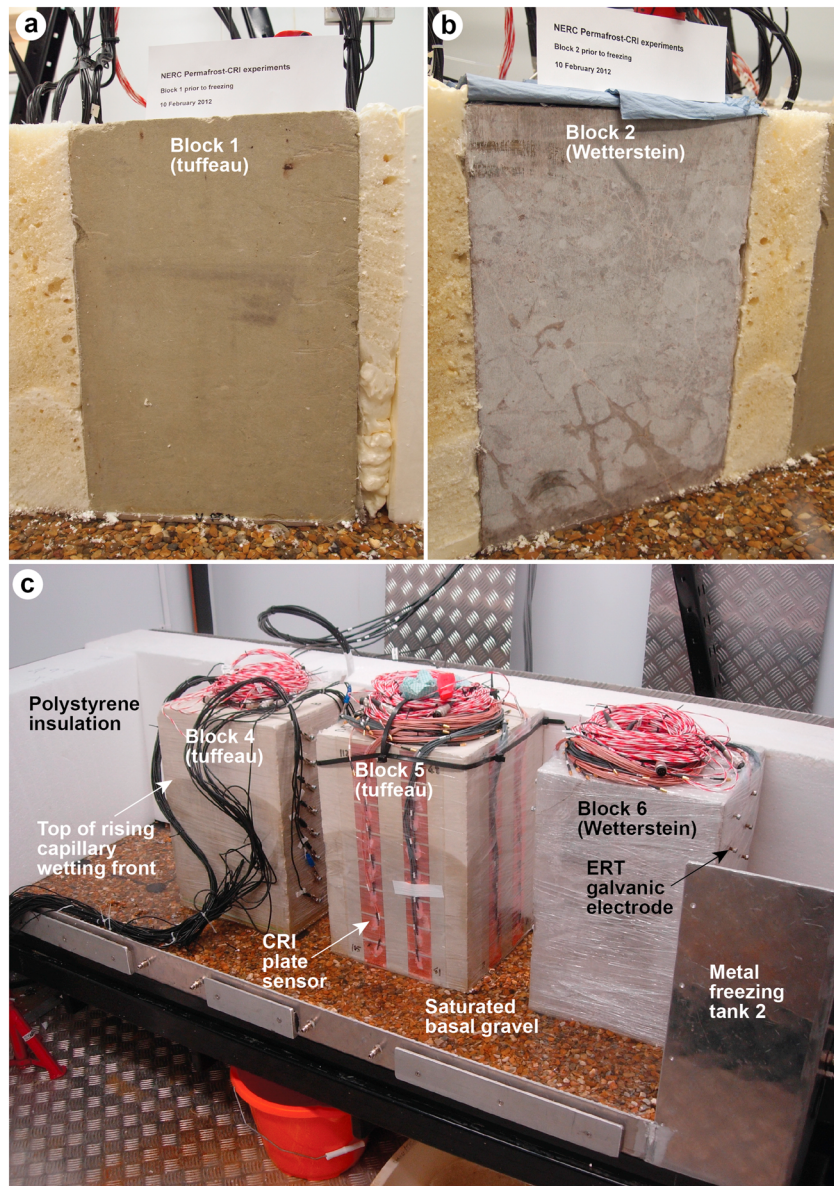
Figure 1. Instrumented blocks resting on water-saturated gravel prior to initial freezing. (a) Block 1 (tuffeau) wetted through by capillary rise. No macroscopic cracks are visible. (b) Block 2 (Wetterstein limestone), with irregular wetting front extending along cracks near base of block. (c) Blocks 4 to 6 within tank 2 (seasonal freezing). CRI plate sensors are installed on the sides of block 5 and ERT galvanic electrodes in the sides of blocks 4 and 6.

of freezing and thawing of moist rock subject to varying degrees of frost weathering. The capacitive methodology, referred to as capacitive resistivity imaging (CRI), uses low-frequency impedance measurements across permanently installed multisensor arrays [*Kuras et al.*, 2006], emulating the well-established ERT methodology, but removing the need for galvanic contact between the sensors and frozen soils or rocks.

We applied a monitoring strategy based on geoelectrical tomography to controlled laboratory experiments simulating permafrost growth, persistence, and thaw in bedrock. Frost weathering was monitored by measuring heave and microseismic activity and by visually observing macrocracks. Our objectives are to explain and present results about rock fracture, geoelectrical monitoring, and microseismic events and to evaluate the performance of CRI beside conventional ERT.

2. Materials and Methods

2.1. Monitoring Strategy

Our monitoring strategy relied on instrumenting multiple rock samples with geoelectrical sensor arrays in order to compare the relative merits of the ERT and CRI techniques in different settings. This allowed us to assess the influence of rock type, freezing regime, weathering status, and the performance of different cross-sample sensor geometries. Experimental control was provided by simultaneous and continuous measurement of vertical rock temperature profiles, surface heave and settlement, and liquid water content in all rock samples, except where there was a risk of the simultaneous measurements interfering with each other or with the geophysical monitoring. The experiments were carried out in the cold room of the Permafrost Laboratory at the University of Sussex. This facility is designed for the physical modeling of permafrost conditions in rock or soil by simulating the effect of different natural freezing regimes.

2.2. Rock Types and Sample Preparation

The rock types used were tuffeau and Wetterstein limestone. The tuffeau is a siliceous and texturally uniform chalk of Upper Cretaceous (Turonian) age, commonly used as a building stone in France. It was selected because it is frost-susceptible and therefore prone to macrocracking [*Murton et al.*, 2001, 2006], allowing us to evaluate its geoelectrical and microseismic response as crack networks evolved. Its physical properties are detailed in *Murton et al.* [2000]. Its porosity measured under vacuum is about 47%. The compressive strength varies from 0.53 to 9.24 MPa and tensile strength from 0.07 to 1.07 MPa. Four samples of tuffeau were obtained from the Lucet limestone quarries, L'Epinay Brézé, near Saumur, in the Loire Valley, France. Prior to the experiments the samples lacked visible evidence of macroscopic cracks or other forms of weathering (Figure 1a).

The Wetterstein limestone is a relatively uniform and isotropic fine-grained (algal) limestone deposited in lagoonal back-reef conditions during the Middle Triassic (Ladinian). It represents a very tough Alpine limestone and forms rock faces such as the Zugspitze North Face, some more than 1000 m high. The Wetterstein limestone was selected because it represents the natural fractured bedrock on which a CRI system might be applied in the field. Wetterstein limestone has also been the host rock for temperature-calibrated permafrost ERT field measurements at the Zugspitze summit [*Krautblatter et al.*, 2010]. Previous laboratory testing of similar limestone at the sample location yielded a porosity of $1.31 \pm 0.22\%$ and a permeability of $4.48 \pm 0.11\,\mu D$, with calcite contents of 99% or more [*Krautblatter*, 2009]. Two samples were cut from a representative and relatively intact, unweathered boulder (about $1\,m^3$) collected at the foot of the Zugspitze North Face. The samples contained macroscopic fractures (Figure 1b).

The rock samples were sawn into six rectangular blocks measuring 300×300 mm wide and 450 mm high, a size sufficiently large to monitor freezing and thawing and simulate almost at field scale rock fracture by ice segregation [*Murton et al.*, 2001, 2006]. Blocks 1, 3, 4, and 5 comprised tuffeau, and blocks 2 and 6 comprised Wetterstein limestone. All were air-dried under ambient laboratory conditions for several months.

The tuffeau blocks, once dry, were drilled prior to inserting sensors into them. Drill holes were 4 mm in diameter and 50 mm long for temperature sensors, 3 mm in diameter and 150 mm long for liquid water sensors, and 4 mm in diameter and 10 mm long for ERT galvanic electrodes. The location and number of holes for the blocks are shown in Figure 2. CRI sensor arrays made from copper foil were attached to transparent cellulose acetate film sheets (cut to cover approximately 80% of the sample faces) and mounted onto the rock surface by using spray adhesive. This was done for the sides of blocks 3, 5, and 6 (Figures 1c and 3), which were then wrapped in low-density polyethylene ("cling film") to protect the CRI sensor arrays and to minimize lateral movements of water into or out of the blocks. The temperature and water sensors were inserted into the blocks, grouting the interior ends of the holes with drill cuttings (chalk powder) and sealing their exterior ends with a vinyl-based filler containing calcite ("Polyfilla"). Stainless steel M5 machine screws were used as galvanic electrodes; these were dipped into conductive contact grease and screwed into the predrilled holes so as to establish and maintain good galvanic contact with the rock matrix.

The Wetterstein blocks, unlike the tuffeau blocks, had a low porosity and contained preexisting cracks, properties that we considered would impede wetting by capillary rise, and so we wetted the Wetterstein blocks by submergence. The samples were submerged in a water-filled container for several days, while the water level
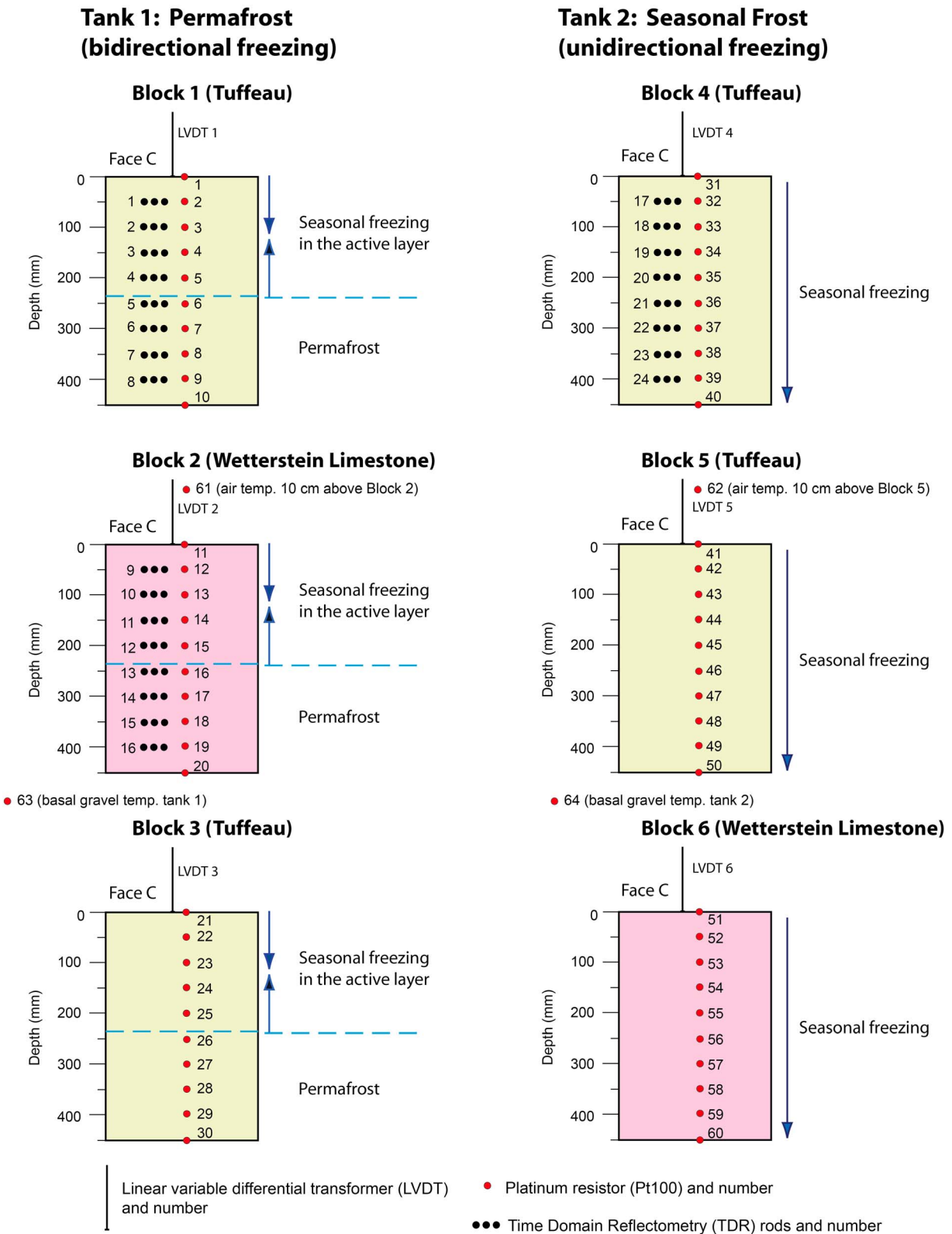
Figure 2. Vertical view of sensor locations for measuring heave (by LVDTs), temperature (by Pt100s), and volumetric unfrozen water content (by TDR).
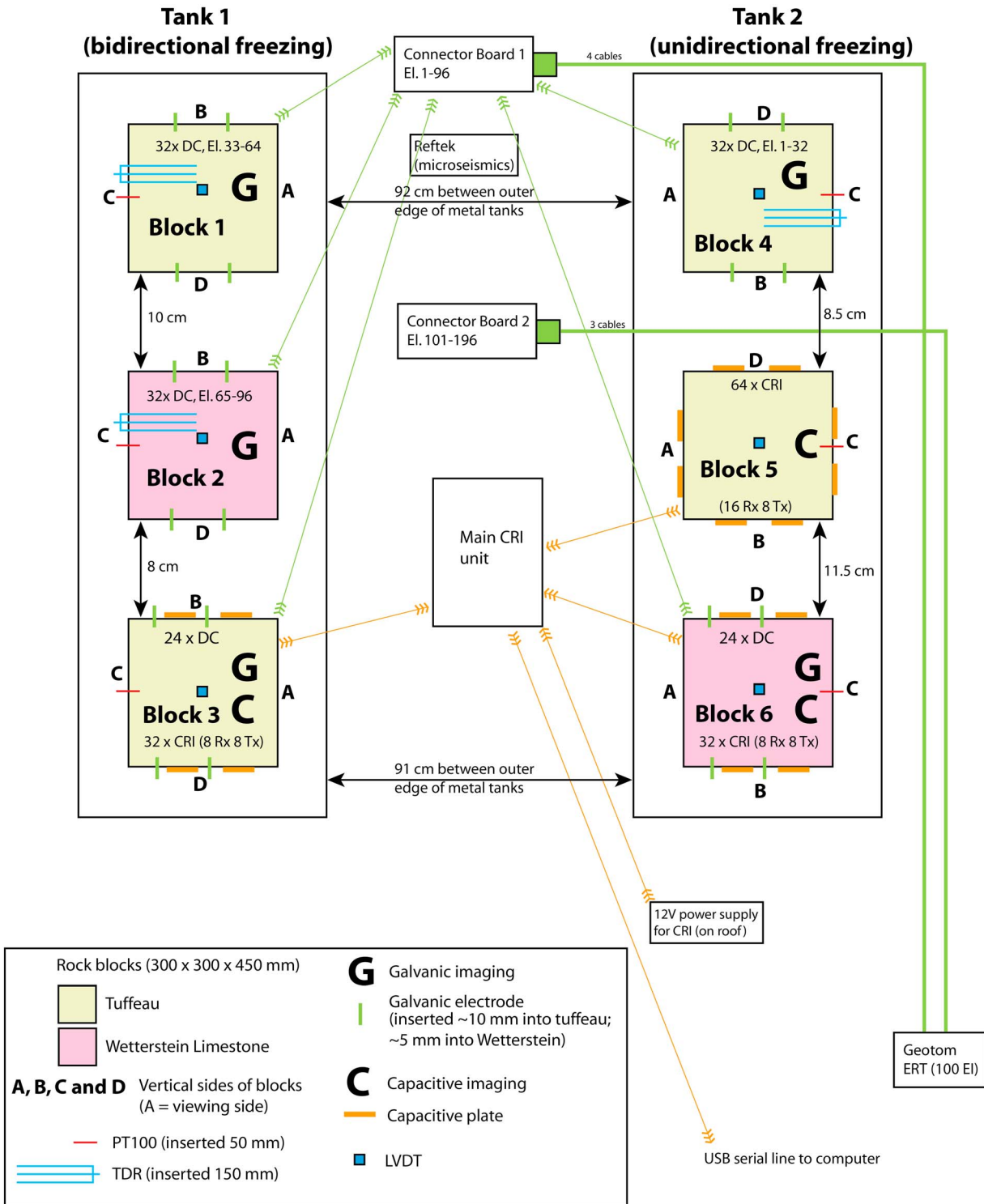
Figure 3. Plan view of experimental setup within the cold room. Not drawn to scale.

dropped by about 10 mm as the rock absorbed water. After the blocks were taken out of the water, the CRI sensor arrays were mounted onto the sides of blocks 2 and 6 by the same method as that described above. Immediately afterward the blocks were wrapped in cling film to minimize drying. Finally, the blocks were drilled and instrumented as per the tuffeau blocks (Figures 2 and 3). The cling film was removed from

beneath the blocks just before they were placed on the wet gravel, so that, as with the tuffeau blocks, cryosuction could draw up water during initial downward freezing of the block 6 and repeatedly during freezing of block 2.

2.3. Freezing System

The freezing system in the cold room used two aluminum tanks, each with an internal length, width, and height of 1895 × 750 × 500 mm, respectively (Figures 1c and 3). Tank 1 contained blocks 1 to 3 and experienced bidirectional freezing and unidirectional thawing to simulate an active layer above near-surface permafrost. Downward freezing resulted from chilled air circulating the cold room, and upward freezing resulted from a thermostatically controlled eutectic cooling plate (manufactured by FIC, model EFR 1570) measuring 1490 mm long, 690 mm wide, and 53 mm high, beneath the tank. Downward thawing occurred under ambient air temperature in the cold room, when the inflow of chilled air ceased and warm air entered from the surrounding laboratory. The space between the blocks and the tank walls was insulated with expanded polystyrene and expanding polyurethane foam to minimize lateral heat transfer during the experiment (Figure 1). Tank 2 contained blocks 4 to 6, which froze and thawed completely during each freeze-thaw cycle in order to simulate seasonal freezing and thawing in the absence of permafrost. The cooling plate beneath the tank was insulated to limit upward freezing, but some upward freezing did occur (section 3.1). Thawing was bidirectional (upward and downward), simulating natural thawing of seasonally frozen ground.

Both tanks contained a horizontal layer of fine gravel, about 100 mm thick, above their base. The gravel contained serpentine copper pipe through which water could circulate to wet, warm, or drain the gravel. The six blocks were placed on hard plastic feet that extended through the gravel to keep the blocks stable. Then water entered the gravel through the serpentine pipe, until the water table was 10–30 mm above the top of the gravel and the bottom of the blocks resting on the gravel surface. Capillary rise wetted the four tuffeau blocks within 3 days, and the rising wetting front in blocks 4 and 5 is shown in Figure 1c.

All six blocks initially froze from the surface downward. Thereafter, basal cooling from the plate beneath tank 1 maintained permafrost in the lower part of blocks 1 to 3 during most of the experiment, while the upper part of the blocks experienced bidirectional freezing, downward from the top and upward from the permafrost table. By contrast, blocks 4 to 6 thawed and froze completely during each cycle. The experiment lasted for 859 days, during which 28 freeze-thaw cycles were monitored, prior to freezing of the blocks at the end of the experiment. Each cycle consisted of a freezing period (with air temperatures <0°C) and a thawing period (air temperatures >0°C). Freezing periods varied in duration between 2.16 and 40.10 days and thawing periods between 1.91 and 108.80 days. Freezing periods and thawing periods varied in duration to test the influence of cycles of different length. In addition, malfunction of the basal cooling plate resulted in some extended periods of freezing and thawing. Active-layer thicknesses (ALTs) in blocks 1 to 3 were obtained by linear interpolation between temperature measurements to determine the maximum depth of penetration of the 0°C isotherm during thawing periods. A few of the ALT values are approximate due to gaps in data acquisition. Macrocracks visible in the outer sides of the blocks were photographed and measured. The blocks were then left to thaw before being encased in fibreglass, to protect them during handling, and then sawn vertically in half with a circular diamond saw to reveal macrocracks visible in an internal face.

2.4. Geophysical Instrumentation and Data Acquisition Protocol
2.4.1. Capacitive Sensors and CRI Instrumentation

Our use of capacitive sensors introduces a new technology concept for the noninvasive volumetric geophysical imaging and routine temporal monitoring of hard rock materials and engineered structures. In a recent numerical simulation study [*Uhlemann and Kuras*, 2014], we demonstrated the feasibility of making multisensor CRI measurements for the 3-D imaging of cuboidal rock samples at laboratory scale. The fundamental theory of capacitively coupled resistivity measurements is described by *Kuras et al.* [2006]. For the present laboratory experiment, we used prototype multisensor CRI instrumentation developed at the British Geological Survey (BGS), which can address a total of 128 sensors and allow the automatic selection of quadrupoles comprising two current injection sensors and two potential measurement sensors out of a set of 64 for each sensor type. Measurements of the complex transfer impedance can be scheduled according to a predefined protocol (sequence of quadrupoles), thus allowing the automated and routine acquisition of

Table 1. Data Acquisition Parameters and Schedule for Environmental and Geophysical Measurements

Method	No. of Sensors/Measurements	Sampling Frequency	Measurement Duration
Temperature	10 per block, 6 blocks	Every 10 min	Instant
LWC	8 per block, 3 blocks	Every 10 min	Few seconds
Heave	1 per block, 6 blocks	Average of 30 values over a 10 min period	Instant
ERT	1028 resistance measurements; 32 sensors per block on blocks 1, 2, and 4; 24 sensors per block on blocks 3 and 6	3 times over a 24 h period	~81 min
CRI	1032 impedance measurements; 32 sensors per block on blocks 3 and 6; 64 sensors on block 5	3 times over a 24 h period	~12.5 min
Microseismic	1 geophone per block, 6 blocks	1 kHz	Continuous

resistivity data sets. A quasi-static estimate of the apparent resistivity ρ_a is extracted by evaluating the in-phase component of the transfer impedance [*Kuras et al.*, 2006]

$$\rho_a \approx \frac{\text{Re } U}{\hat{I}} \times K^{dc}$$

where Re denotes the real part (in-phase component), $\hat{I}$ is the injected current, U is the observed potential, and K^{dc} is the DC geometric factor.

We instrumented the rock samples with capacitive sensors made from 50×50 mm squares of dead soft copper foil backing (3M 1181 Tape), arranged in vertical columns of eight sensors each with a mutual spacing of 5 mm (55 mm separation between square centres), with two columns placed side-by-side (100 mm separation between column centres) on opposite sides of the sample (Figure 1c). The total thickness of the copper foil sensors including the adhesive layer was 66 μm. Blocks 3 and 6 were instrumented on two opposing faces only (32 sensors each, which gave eight current and eight potential dipoles), whereas block 5 was instrumented on all four faces (64 sensors, which gave 16 current and 16 potential dipoles) (Figure 3).

These capacitive sensor arrays were used to collect bipole-bipole impedance data on the three instrumented blocks consecutively. Data acquisition was scheduled 3 times over a 24 h period, leaving at least 6 h intervals between successive acquisition events (Table 1). Only cross-sample array styles were used in accordance with *Uhlemann and Kuras* [2014], and a transmitter frequency of 15 kHz was employed. A total of 344 impedance measurements each were made on blocks 3 and 6, while 688 measurements were made on block 5.

2.4.2. Galvanic Sensors and ERT Instrumentation

Conventional ERT monitoring using DC resistivity measurements with galvanically coupled sensors was carried out alternately with the capacitive measurements described above. We used a multielectrode multichannel resistivity meter (Geotom MK4E200 manufactured by GEOLOG 2000, Germany), which is capable of making stable resistance measurements in highly resistive environments using relatively low input power and very small transmitter currents (minimum of 0.1 μA).

The geometry of the electrode arrays mirrored that of the capacitive sensors. ERT electrodes were arranged 55 mm apart in vertical columns of eight electrodes each, two columns being placed 100 mm apart on opposing faces of the samples (Figure 1c). Blocks 1, 2, 3, 4, and 6 had ERT electrodes on two opposing faces only (32 electrodes each); block 5 did not have any ERT electrodes (Figure 3). On blocks 3 and 6 the ERT electrodes were interspersed with the capacitive sensors by laterally offsetting the ERT electrode columns to fit into the available space on the vertical sample faces.

Measurements on the ERT sensor arrays were essentially analogous to those made with the capacitive technique. However, the design of the Geotom resistivity meter allowed automated collection of reciprocal resistance data, where current and potential dipoles are swapped and the measurement is repeated [e.g., *Loke et al.*, 2013]. This was not possible to automate with the prototype CRI instrument, which required manual swapping of connections in order to perform reciprocal acquisition.

ERT data acquisition was scheduled 3 times over a 24 h period, leaving at least 6 h intervals between successive acquisition events (06:00, 12:00, and 18:00 h; Table 1). A total of 1028 resistance measurements each were made on blocks 1, 2, 3, 4, and 6, which included reciprocals. The total measurement sequence on all five blocks took approximately 81 min to complete. Occasional failures of ERT data acquisition (and resulting gaps
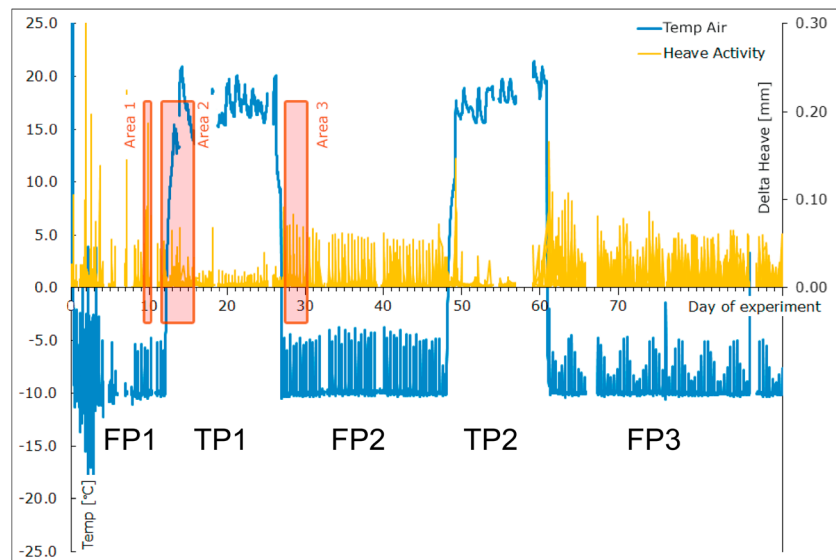
Figure 4. Training slots of rapid heave which were used for calibrating microseismic filtering and event detection during freezing periods and thawing periods 1–3.

in the apparent resistivity time series) are attributed to circumstances where contact impedances were too high to obtain galvanic measurements.

2.4.3. Microseismic Sensors and Instrumentation

Microseismic signals were collected by using a Reftek RT130 6 channel high-resolution data logger. Six 4.5 Hz 1-D geophones were positioned on top of the six rock blocks (i.e., one geophone per block) and recorded with a frequency of 1000 samples per second (sps). The microseismic recorder operated during three freezing and two thawing periods in April to June 2012. To filter out signal from the enormous amount of seismic data collected with 1000 sps we defined training time slot and preselection criteria. Three training time slots were chosen according to pronounced and prolonged heave activity of the rock sample (Δheave >0.05 mm/ 10 min) (Figure 4). As signals are transduced from one sample to the neighboring sample with a certain time delay and attenuation, the seismic signals recorded during the training slots were preselected according to the following criteria: (i) seismic events do not happen on all blocks at the same time (i.e., noise from labora-tory checks and ventilation onset), (ii) a time difference of signal onset occurs from one block to the others; (iii) a clear intensity loss occurs from one block to the others, and (iv) the waveform of events clearly differs from that of recorded noise.

We then used spectral analysis based on Fourier decomposition to identify the frequency band associated with noise, calibrated in a 24 h time slot prior to the onset of the temperature forcing as well as the frequency band associated with signals. To filter out low frequencies we applied a high-pass Butterworth filter, which has only little effect on the filtered signal characteristics. Events were then automatically detected by using a short time average over long time average (STA/LTA) trigger algorithm, where the amplitude of the short time seismic signal was compared to the long-term average noise. Initial STA/LTA thresholds were 6.5 for trig-gering and 3.5 for detriggering for 0.3 s long STA periods calibrated by using the test data and based on *Vaezi and Van der Baan* [2014]. Events were detected on 52 of 72 recording days.

2.5. Temperature

Rock temperature was measured by cylindrical platinum resistance thermometers manufactured by British Rototherm Co Ltd. The resistors are 100 Ω at 0°C (PT100) and consist of a PR2825 element made to BS EN 60751:1996 Standard, 4 wire, Class A. The element is connected to a silver-plated copper twisted insulated lead 7 m long with 7/0.2 polytetrafluoroethylene core and with PTFE shrink sleeve fitted over each joint and over the final sleeve. The element and connection to the lead are embedded in epoxy and encased in a closed-end tube of 316 stainless steel that is 4 mm in external diameter, 3 mm internal diameter, and 40 mm long. The manufacturer's stated tolerance of the PT100 resistor is ±0.15°C at 0°C. The resistors were
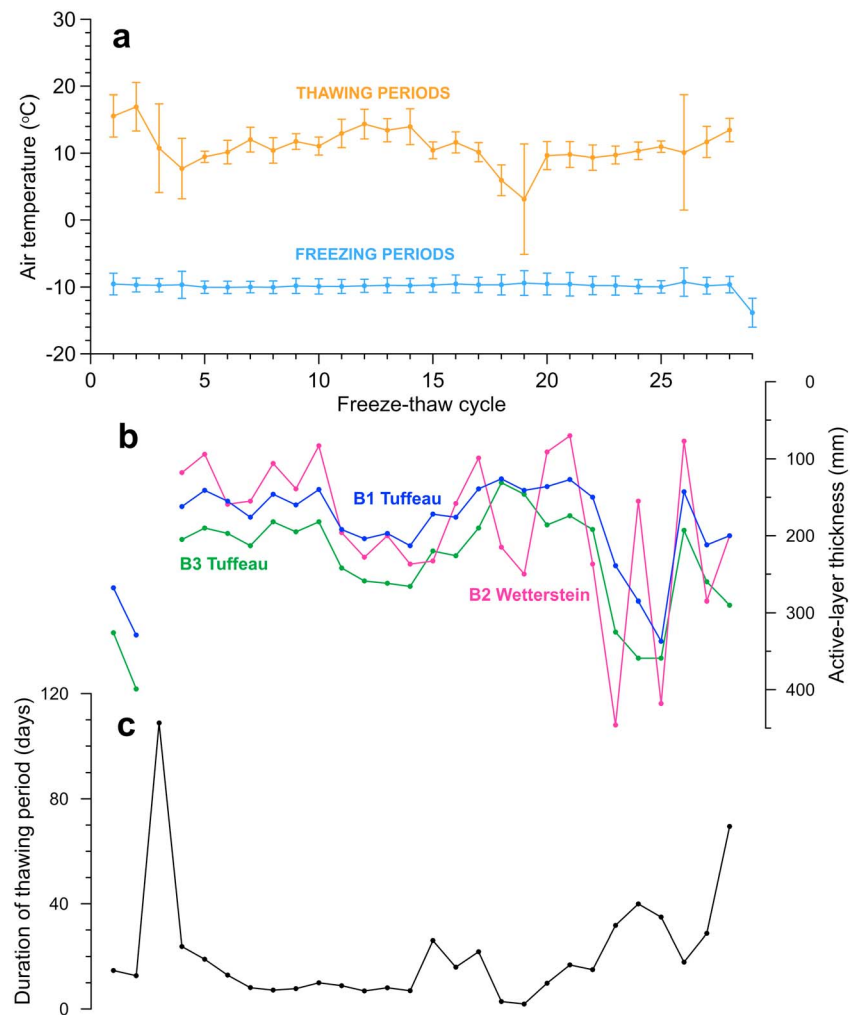
Figure 5. Mean air temperature (±1 SD) of the cold room during (a) freezing and thawing periods, (b) time series of ALT in blocks 1 to 3 during the active layer-permafrost experiment, and (c) duration of thawing periods. Missing values of ALT resulted from complete thaw of block 2 during freeze-thaw cycles 1 to 3 and of blocks 1 and 3 during cycle 3 due to malfunction of the basal cooling plate.

calibrated to an accuracy of ±0.1°C in a mechanically stirred ice-water bath, prior to installing them in the blocks. The precision of the PT100s during the experiment is estimated to be typically ±0.1°C. Rock temperature was measured at 50 mm depth increments from the block surface to the base ($n = 10$ per block), with the PT100s at depths between 50 and 400 mm. The surface (0 mm) and basal (450 mm) PT100s were glued into a shallow groove cut into the block surface and base with an angle grinder. Sensor locations are shown in Figure 2. Additional PT100s measured the air temperature within the cold room. Temperatures were logged every 10 min during the experiment.

2.6. Volumetric Unfrozen Water Content

Volumetric unfrozen water content (θ_u) in the rock mass was measured by time domain reflectometry (TDR) by using a Campbell Scientific TDR100 Time Domain Reflectometer. The unit was connected to 24 stainless steel TDR probes (model CS635, 3-rod probe, rod length 150 mm) via low-loss LMR200DB cable and SDMX50 coaxial multiplexers. Blocks 1, 2, and 4 were instrumented with eight TDR probes mounted in a vertical column at depth separations of 50 mm. The individual probes were oriented horizontally (Figure 2), and their exterior ends were sealed with Polyfilla. TDR data were logged every 10 min with a Campbell Scientific CR800 data logger. TDR probes act as a waveguide, and impedance along the rods varies with the dielectric permittivity of the surrounding rock matrix, including any pore water in liquid or frozen form. As the dielectric

permittivity primarily depends on the amount of water present, θ_u can be inferred from measurements of the elapsed travel time and pulse reflection amplitude. The diameter around the sensor from where the water content is sensed is estimated to be approximately 25 mm. There are three parallel rods in a line, meaning that the rock volume measured has an oblong or ellipsoidal shape. We used the Topp equation [*Topp et al.*, 1980] to calculate θ_u from apparent dielectric permittivity.

2.7. Surface Heave and Settlement

Heave and settlement of the block tops were measured in order to provide an indirect and noninvasive measure of macrocracking, because our previous experiments with tuffeau indicate that macrocracking causes dilation and therefore heave of the rock top. Heave and settlement were measured by six linear variable differential transformers (LVDTs; models LDC2000C and LDC1000C, with captive guided armature) manufactured by RDP Group. Their linearity was ±0.35% of the full range, and their sensitivity exceeded 46 mV mm^{-1}. Each LVDT was calibrated individually with metal slips of known thickness prior to the experiment. The foot of each LVDT rested on a metal stud glued near the center of the top of each block. A seventh LVDT was attached horizontally to the metal frame above tank 2 in order to measure its sensitivity to temperature change.

Logging of heave and temperature was performed with a National Instruments CompactDAQ multiplexed USB data acquisition system (model NI cDAQ-9172) connected to four 32-channel analog input modules (model 9205). The measurement and control system uses LabVIEW software, which was programmed to average 30 values measured during sampling periods of 10 min.

3. Results

3.1. Temperature and Active-Layer Thickness

Air temperature in the cold room had mean values of −9.3 to −13.8°C during freezing periods and 3.1 to 16.9°C during thawing periods (Figure 5a). Active-layer thickness (ALT) varied substantially between blocks and between thawing periods (Figure 5b). In the tuffeau blocks (nos. 1 and 3), ALT varied from 126 to 337 mm (mean = 188 ± 59 mm) in block 1 and from 131 to 399 mm (mean = 236 ± 69 mm) in block 3. The Wetterstein block (no. 2) showed the greatest variation, from 70 to 446 mm (mean = 186 ± 97 mm). Factors influencing ALTs included the mean air temperatures during thawing periods (Figure 5a) and the duration of thawing periods (Figure 5c).

Bidirectional freezing and unidirectional thawing are shown for the first few freeze-thaw cycles during days 0–70 of the active layer-permafrost experiments in tuffeau blocks 1 and 3 and in Wetterstein block 2 by the contoured isotherms in Figures 6a–6c. Temporary failure of the basal cooling plate around days 58–61 led to complete thaw of block B2 and unusually deep thaw of blocks B1 and B3 (Figure 5). In the seasonal frost experiment, all three blocks froze from the top downward as well as from the bottom upward (Figures 6d–6f), the latter attributed to imperfect insulation of the basal cooling plate. The Wetterstein block 6 thawed downward (Figure 6f), whereas tuffeau blocks 4 and 5 also experienced upward thaw, as expected under natural conditions of seasonal frost in the absence of permafrost. The absence of upward thaw of the Wetterstein block 6 is attributed to its low porosity and hence water content; thus, negligible latent heat would have been released during thaw, which facilitated rapid thaw from above rather than from below through the limited basal insulation.

3.2. Volumetric Unfrozen Water Content

The volumetric unfrozen water content (θ_u) in tuffeau blocks 1 and 4 varied substantially between freezing and thawing periods, as illustrated during the first 70 days of the experiments (Figure 7). Freezing periods were characterized by θ_u values of about 0.1 m^3 m^{-3} in both experiments and thawing periods by about 0.2 to 0.3 m^3 m^{-3} in the active layer of block 1 and throughout block 4. Peak θ_u values of 0.41 and 0.45 m^3 m^{-3} briefly developed during early stages of thawing period 1 at 150 mm depth in B1 and B4, respectively. These occurred during phase changes of ice to water and are attributed to rapid drawdown of water by cryosuction into partially frozen rock before the rock at a particular depth had completely thawed. In permafrost of block 1, θ_u values during thawing period 1 increased marginally to about 0.11 m^3 m^{-3} (depths of 300, 350, and 400 mm in Figure 7a), while ALT reached 268 mm. However, during the final 2–3 days of thawing period 2, as ALT approached 329 mm, θ_u values increased rapidly to 0.18 and 0.15 m^3 m^{-3} at depths of 350 and 400 m, respectively, indicating that the warm permafrost contained substantial amounts of unfrozen water.
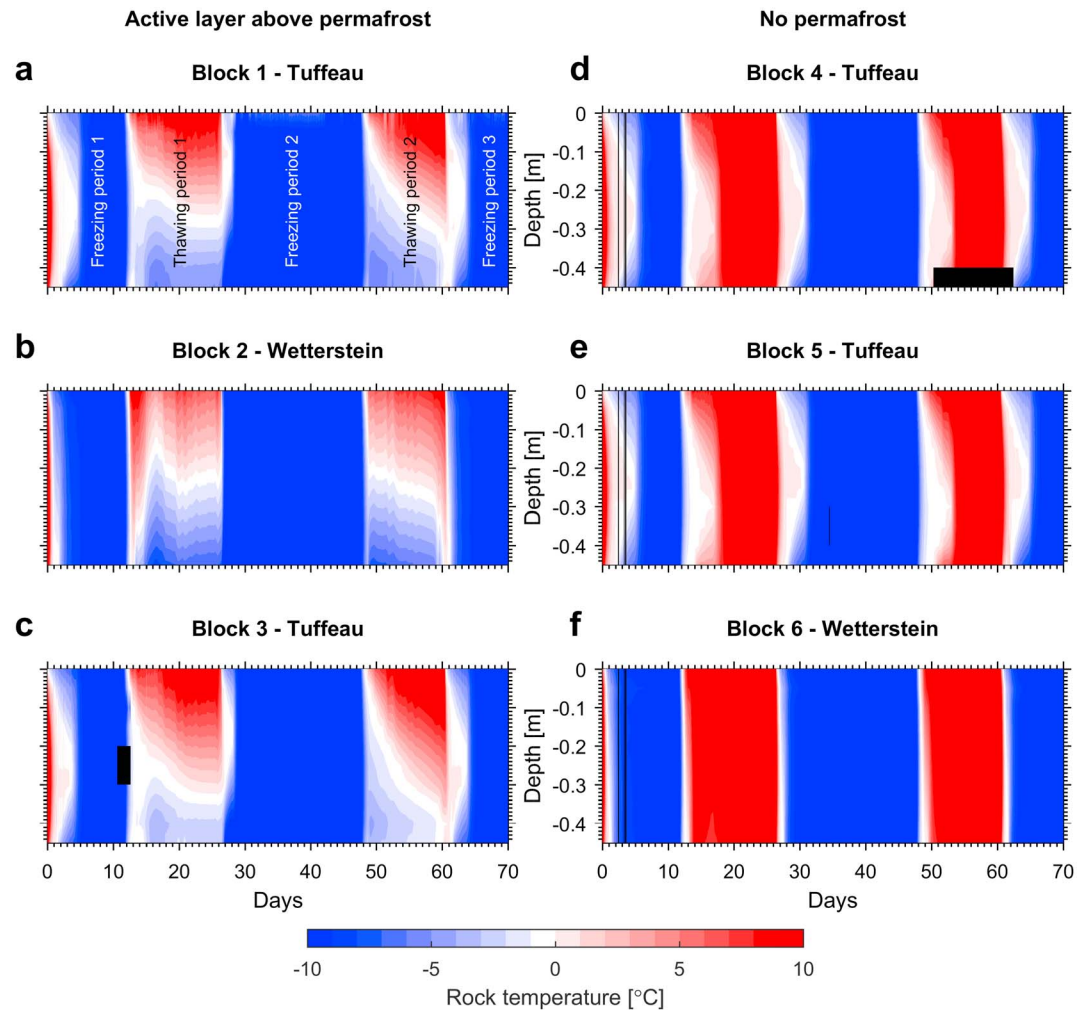
Figure 6. Temperature time series in blocks 1 to 6 during the first 70 days of the experiments, with (a–c) bidirectional freezing of an active layer above permafrost, and (d–f) bidirectional freezing and thawing of rock lacking permafrost. Freezing periods and thawing periods are indicated in Figure 6a. The black areas indicate missing or anomalous data, where interpolation is inappropriate.

Unfortunately, measurement of θ_u after about day 100 in tuffeau blocks 1 and 4 failed and was not successful in Wetterstein block 2 throughout the experiment. By the end of the experiment some of the TDR rods extracted from tuffeau block 4 were highly corroded, with holes up to a few millimeters long in them. The reason for the failure of TDR to measure unfrozen water content for the Wetterstein block is not known for certain. But, as suggested by *Sass* [2005], TDR may be better suited for homogeneous, porous rocks such as sandstone and tuff [*Hokett et al.*, 1992], as well as the tuffeau in the present experiments. Possibly, the heterogeneity caused by preexisting cracks in the Wetterstein block, as well as its low porosity, may have contributed to the failure. Although TDR measurements in rock can be affected by movement of water along TDR rods, for example, following rainfall [*Sass*, 2005], we did not identify this as a problem because our experiments did not involve sudden wetting of the rock faces in which the rods were inserted.

The cause of small peaks in θ_u at some depths shortly before freezing (e.g., days 2 to 3 in blocks B1 and B4 and days 28 and 62 in B4) is uncertain. An explanation in terms of pore water pushed ahead of a freezing front into unfrozen limestone and dolostone, whose low porosity (1–10%) is mainly due to cracks and narrow fissures [*Sass*, 2004], is thought to be unlikely for two reasons. First, ice segregation and therefore cryosuction, rather than water expulsion, is indicated by the occurrence of segregated ice within macrocracks, as discussed below in sections 3.4 and 4.1. Second, the expulsion of water ahead of a freezing front is most likely to occur
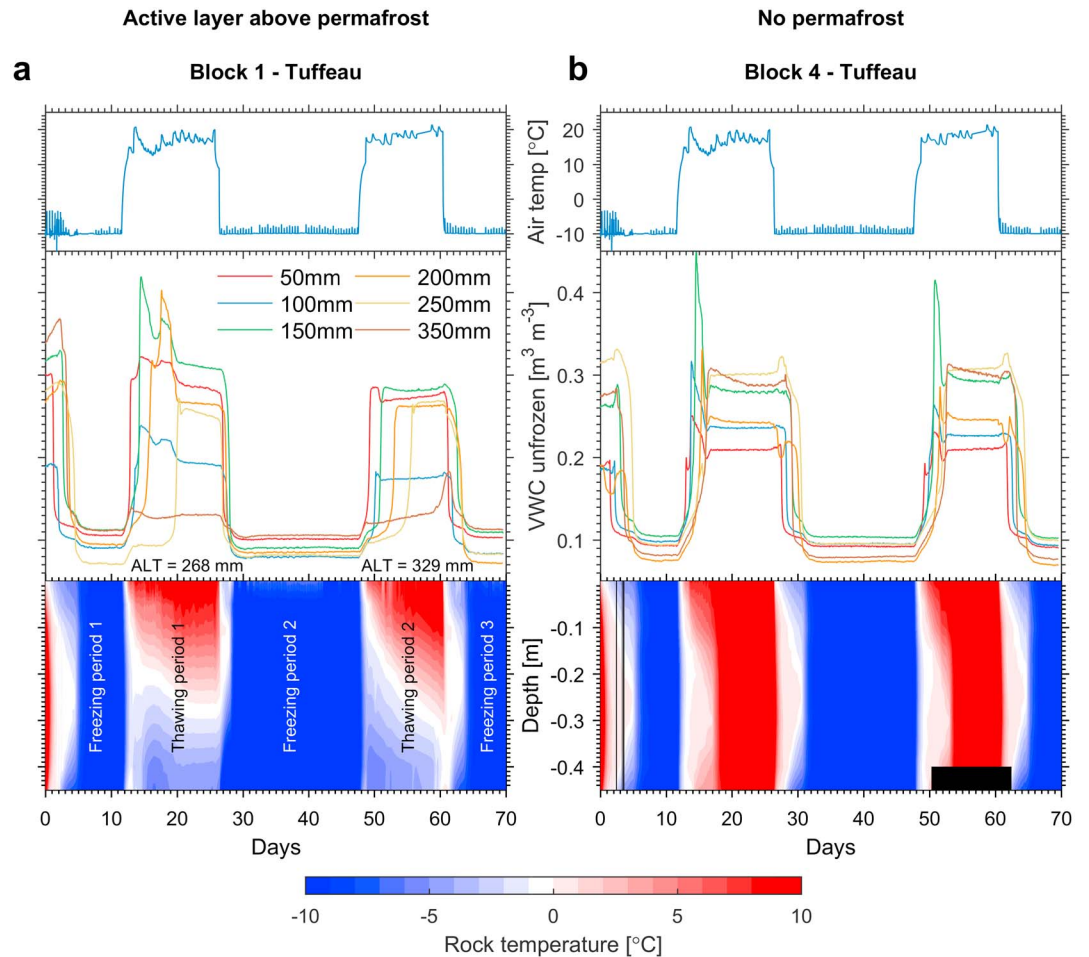
Figure 7. Time series of air temperature, volumetric unfrozen water content, and rock temperature in tuffeau blocks 1 and 4 during the first 70 days of the (a) active layer-permafrost experiment and (b) seasonal frost experiment. Depths of water content measurements are indicated by colored lines. Freezing periods and thawing periods indicated in Figure 7a.

in coarse-grained porous media such as saturated sand and gravel, as associated with hydrostatic pingos [*Mackay*, 1998], and along macroscopic cracks and fissures in low-porosity rocks, as discussed by *Sass* [2004]. In both coarse-grained porous media and along cracks in rocks the magnitude of pore water expulsion can overwhelm the opposite process of cryosuction. An alternative explanation for the small peaks in θ_u may relate to changes in electrical conductivity caused by solute rejection during freezing, but this requires further study.

3.3. Heave

Heave of the block tops varied according to rock type and freezing regime. Tuffeau blocks 1, 3, and 4 showed a net heave of 7.6 to 13.4 mm during the experiment, whereas Wetterstein block 2 heaved 1.8 mm and Wetterstein block 6 heaved 0.2 mm (Figure 8). In the active layer-permafrost experiment, tuffeau blocks 1 and 3 heaved progressively during the middle to late stages of many thawing periods, whereas in the seasonal frost experiment tuffeau blocks 4 and 5 tended to settle during the late stages of thawing periods.

The heave behavior of tuffeau blocks 4 and 5 differed substantially. Block 4 showed the greatest magnitude of heave and settlement during freeze-thaw cycles and the second greatest amount of net heave of any block (Figure 8). The range and heave and settlement over individual freeze-thaw cycles were up to ~5 mm. The net heave measured over the experiment was 12.8 mm, which is a conservative estimate because the LVDT reached the top of its travel during some cycles (indicated in Figure 8 by the flat tops during some cycles).
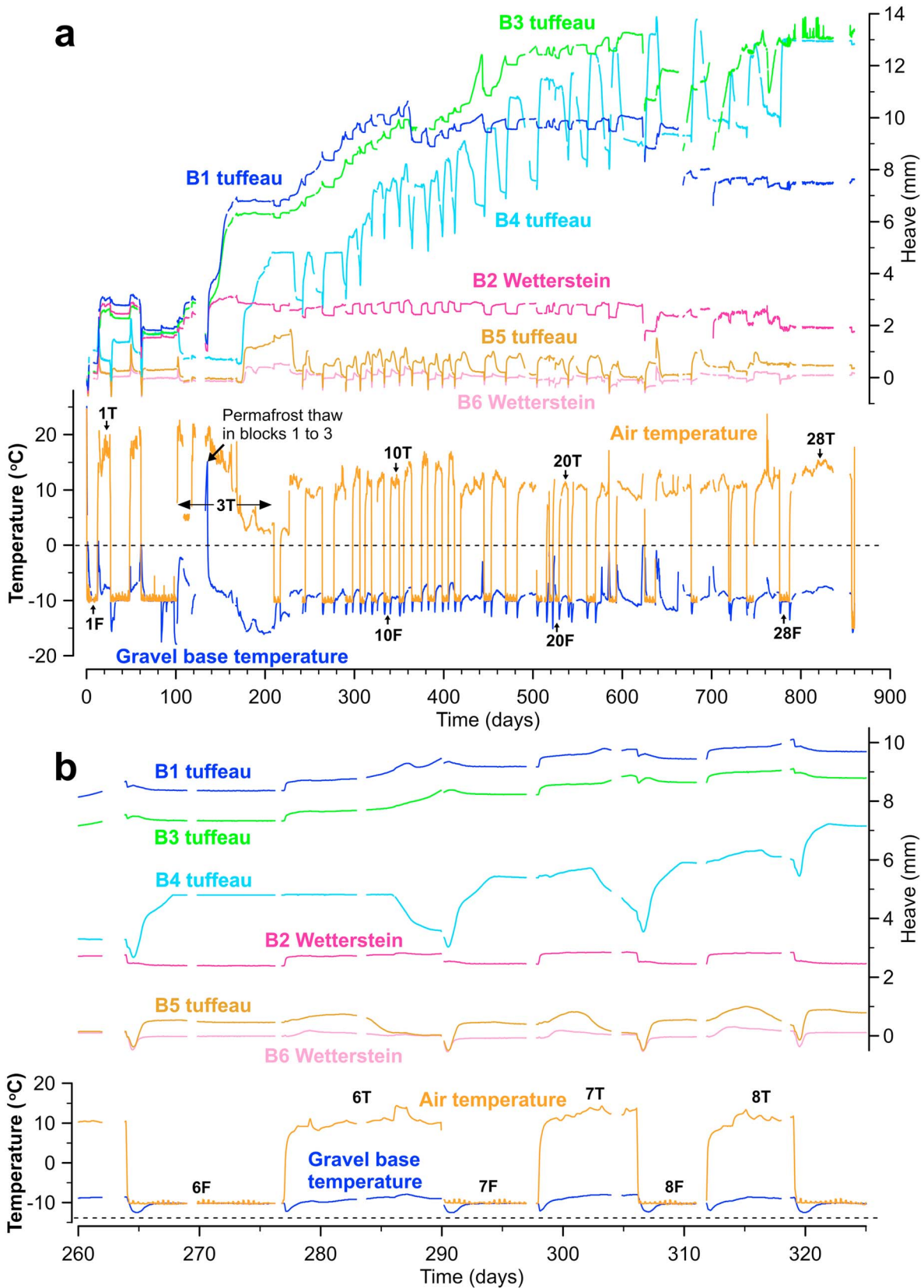
Figure 8. (a) Heave of blocks 1 to 6, air temperature of cold room, and gravel base temperature in tank 1 during the experiments. "1 F" to "28 F" indicate freezing periods 1 to 28, and "1 T" to "28 T" indicate thawing periods. (b) Detailed plot of heave through freezing period 6 to thawing period 8.
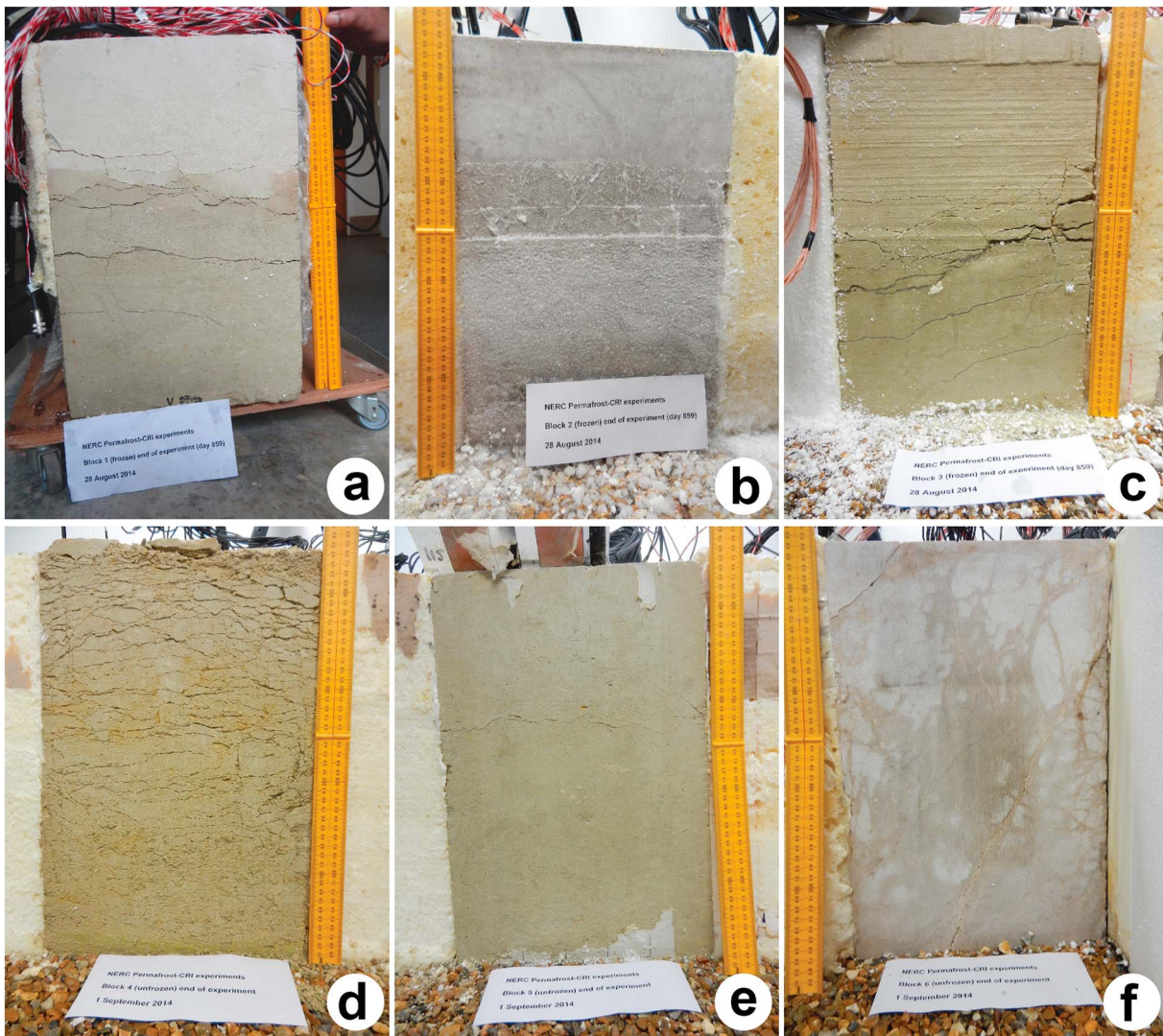
Figure 9. (a–f) Macrocracks in vertical side A of blocks 1 to 6 at the end of the experiments. Figures 9a–9c are the frozen blocks, with segregated ice in the cracks. Figures 9d–9f are the thawed blocks. Ruler in centimeters.

In contrast, block 5 had a net heave of less than 0.4 mm and showed heave-settlement ranges of typically 1–2 mm during freeze-thaw cycles.

3.4. Macrocracks and Weathering

Macrocracks developed in all four tuffeau blocks during the experiments. The cracks were mostly horizontal to subhorizontal in orientation (Figures 9 and 10). Some vertical to subvertical cracks also formed, and in the case of the internal saw-cut face in tuffeau block 5 were dominant (Figure 10d).

The depth of cracks varied according to the freezing regime. In blocks with an active layer above permafrost (1 and 3), cracks were concentrated in the upper part of the permafrost and the lower part of the active layer (Figures 9a, 9c, and 11a). But in blocks lacking permafrost (4 and 5), cracks occurred to greater depths, reaching almost the bottom of both blocks (Figure 11a). Remarkably, cracks were pervasive throughout block 4 (Figures 9d and 10c), whereas in block 5 a few horizontal cracks were observed in the upper half of the outer side (Figure 9e) and a subvertical crack was prominent on an internal face (Figure 10d). Block 4 also showed signs of color mottling, with patches of orange brown discoloration on both the external and internal sides (Figures 9d and 10c).
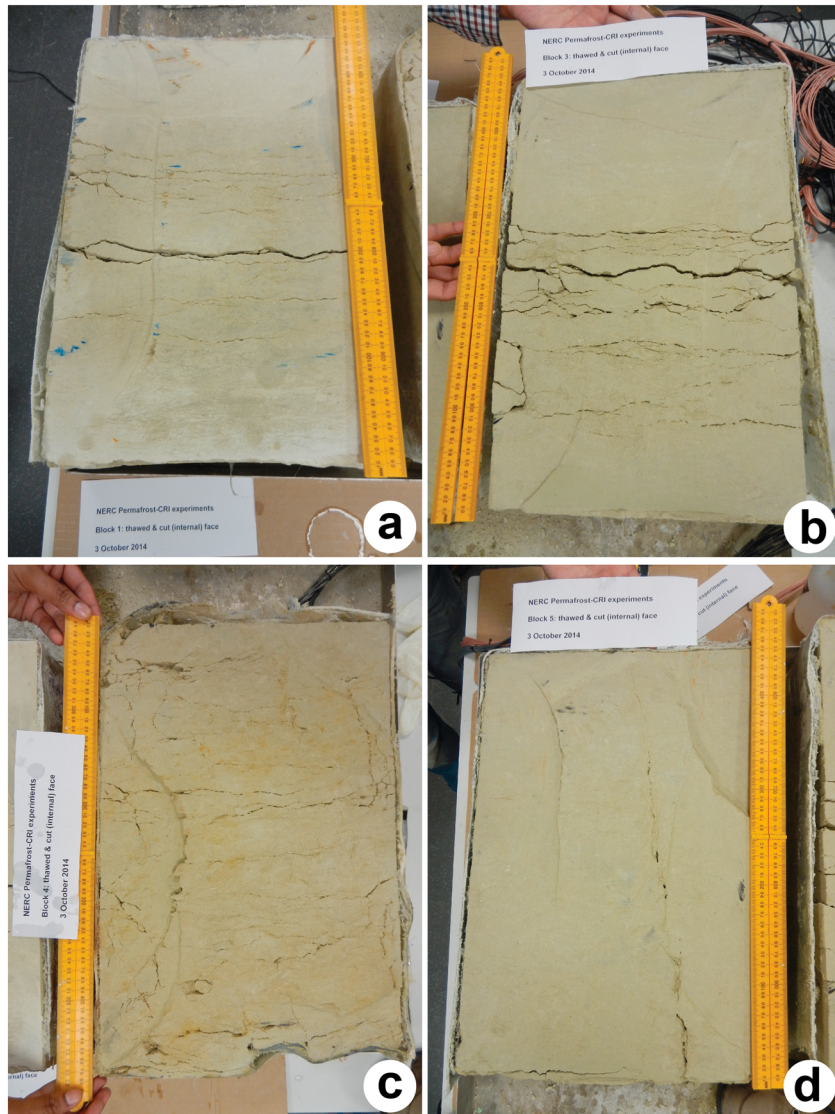
Figure 10. Macrocracks visible within an internal vertical saw-cut face of tuffeau blocks (a) 1, (b) 3, (c) 4, and (d) 5. Blocks are encased in a layer of fiberglass. Ruler in centimeters.

The number of cracks observed in vertical traverses across the blocks also varied, particularly in the experiment lacking permafrost. In blocks 1 and 3 the median numbers of cracks were 8 and 11, respectively. In block 5, the median value was 4 cracks, and in block 4 it was 19. The latter number, however, is likely an underestimate because it was based on examination of the internal cut face (Figure 10c), when it was not possible to remove saw-generated dust from all the cracks, and earlier measurement of the external vertical side A during thaw cycle 27 revealed a median value of 59 cracks; a value more consistent with the abundant cracks shown in Figure 9d.

3.5. Geoelectrical Data

We focus here on our overarching goal to assess the suitability of geoelectrical methodologies for monitoring freeze-thaw processes in contrasting rock types and under different thermal regimes (permafrost and seasonal frost). We present example data from blocks 3 and 6, as these reflect both thermal regimes, both rock types, and are measured with both geoelectrical measurement techniques, therefore allowing direct comparison. The analysis is preliminary and limited to the contact properties associated with CRI and ERT and the apparent resistivity estimates obtained from both techniques.
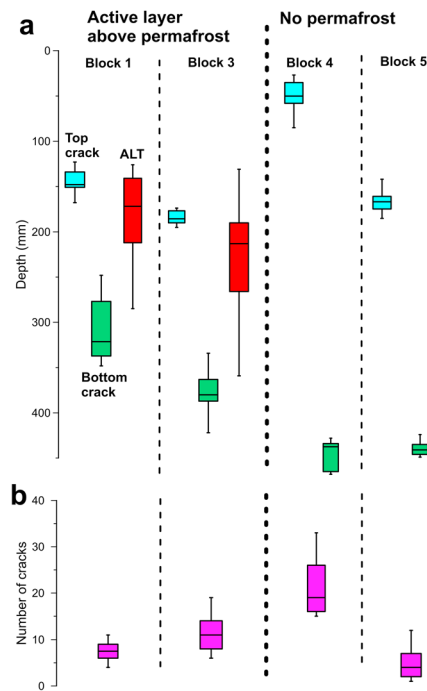
Figure 11. (a) Boxplots of depths to top and bottom cracks observed at the end of the experiments in tuffeau blocks 1, 3, 4, and 5. ALT values for blocks 1 and 3 are also shown. (b) Number of cracks recorded at the end of the experiments. The colored boxes show the interquartile range, the horizontal line within the boxes is the median, and the whiskers extend to the highest and lowest values within 1.5 times the interquartile range.

3.5.1. Electrical Contact Properties

Electrode coupling is a critical parameter and known source of error in geoelectrical measurements, particularly for cryospheric applications [*Doetsch et al.*, 2015; *Tomaškovičová et al.*, 2016]. High contact impedances can severely limit the size of the injectable current or generate unstable potential measurements, thus creating bias in some geoelectrical measurements [*Zonge and Hughes*, 1986; *Ingeman-Nielsen et al.*, 2016]. ERT relies on the galvanic contact between the electrodes and the ground, giving rise to a contact impedance dominated by ohmic resistance. The CRI contact impedance on the other hand is dominated by the capacitive reactance established between the sensor and the ground surface, which in turn is a function of their separation and the dielectric properties of the separating medium [*Kuras et al.*, 2006].

For our experiments, the measurement of contact properties could not be automated with the available ERT and CRI instrumentation, and therefore could not be performed continuously and systematically throughout the experiment. Instead, representative measurements were carried out opportunistically at key stages during the seasonal temperature cycle. Figure 12 shows the distribution of contact impedance magnitude obtained for both the CRI and ERT sensor arrays during thawed and frozen states, respectively. Impedance magnitudes were measured by ERT on block 3 (tuffeau) (Figures 12a and 12b) and on block 6 (Wetterstein) (Figures 12c and 12d). Equivalent CRI measurements were made on blocks 3 (Figure 12e) and block 6 (Figure 12f). The values shown in Figures 12a and 12c were obtained in a thawed state, whereas all other values were measured on frozen rock, which naturally presents the greater challenge for low-frequency geoelectrical techniques.

3.5.1.1. ERT

The ERT electrodes experienced a wide range of contact impedances across the two rock types and the seasonal conditions. At practically all times the impedances were at least 1–2 orders of magnitude higher than for typical ERT installations in soft soils or sediments. In line with expectations, the lowest range of values was observed on tuffeau in a thawed state (median = 62.7 kΩ; Figure 12a), although deeper sensors reaching the permafrost layer experienced higher contact impedances. On the same block, median values were approximately 4 times higher during frozen states (median = 238.5 kΩ; Figure 12b). All values remained below ~300 kΩ at the time of measurement (after the 27th freezing cycle and during the 28th cycle, respectively).
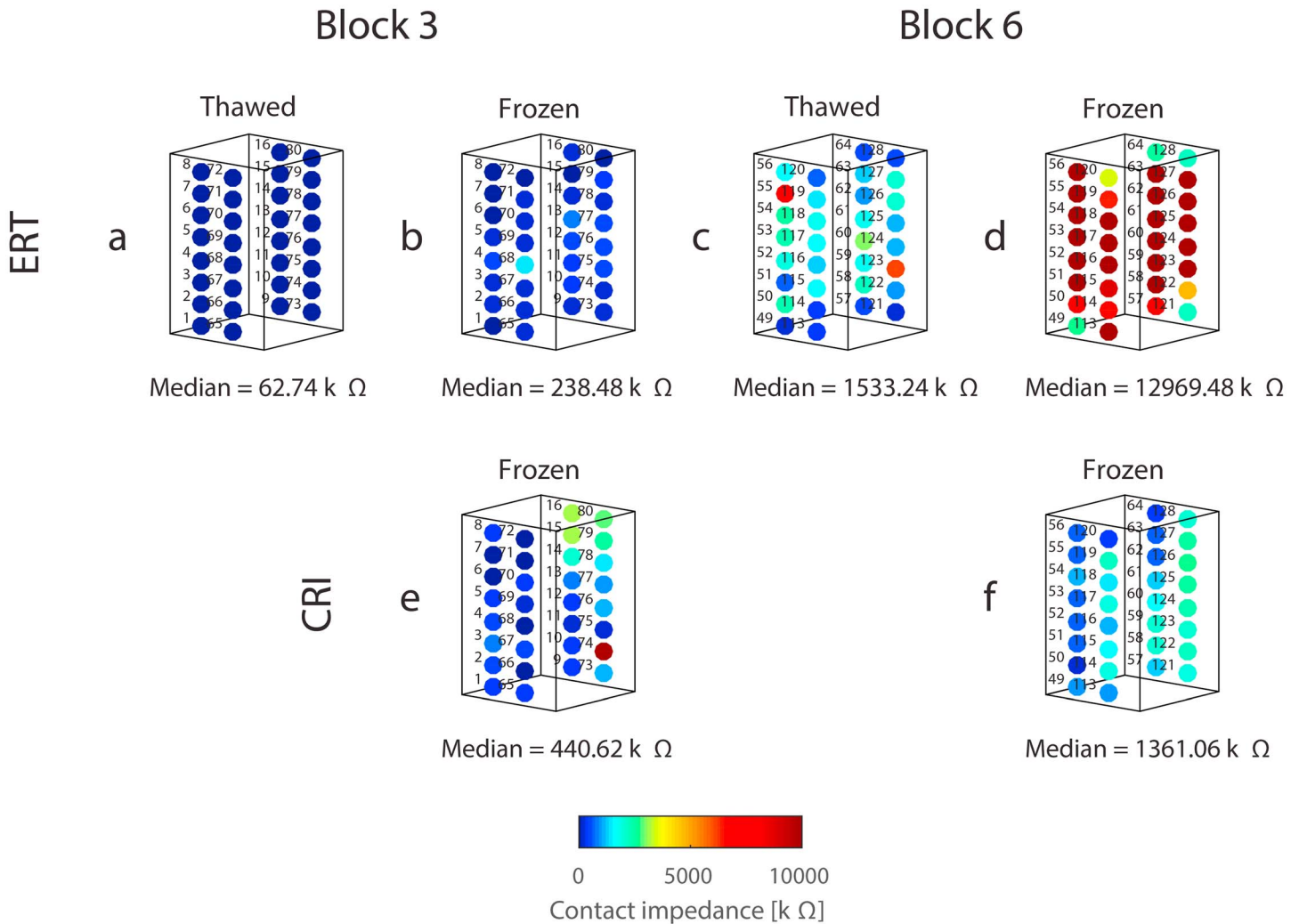
Figure 12. Contact impedance (magnitude) for geoelectrical sensor arrays, measured at representative stages of the freeze-thaw experiments. ERT electrodes on block 3 (tuffeau) in (a) thawed and (b) frozen states; ERT electrodes on block 6 (Wetterstein) in (c) thawed and (d) frozen states. CRI sensors (e) on block 3 (tuffeau) and (f) on block 6 (Wetterstein), both in frozen states. ERT data acquired on 22 May 2014 (thawed state) and 11 June 2014 (frozen state); CRI data acquired on 13 June 2014.

On the Wetterstein limestone, median values observed in thawed states were more than 20 times higher than on tuffeau (median = 1,533 kΩ; Figure 12c), despite the absence of a permafrost layer in block 6. The highest median values occurred in Wetterstein in a frozen state (median = 12,969 kΩ; Figure 12d)—>50 times higher than those observed on tuffeau around the same time. The highest contact impedances observed on Wetterstein were around 15 MΩ. For such poorly coupled sensors, obtaining stable ERT measurements with acceptable noise properties is extremely challenging and often beyond the capabilities of typical survey instrumentation [*Tomaškovičová et al.*, 2016].

3.5.1.2. CRI

Owing to logistical constraints resulting from the prototype nature of the CRI instrumentation, only contact impedance measurements on frozen blocks (but on both rock types) were carried out for CRI. On tuffeau, the CRI sensors experienced median contact impedances of 440.6 kΩ (Figure 12e), which is comparable with the contact impedances seen by ERT under the same conditions (Figure 12b). Some instances of higher CRI contact impedances (sensor nos. 14–16, 78–80, and 74) are attributed to greater separation between individual CRI sensors and the rock surface due to reduced adhesion or increased surface roughness on some sample faces. On Wetterstein limestone, a median value of 1361.1 kΩ was observed (Figure 12f), which is only greater by a factor of ~3 than the tuffeau value. These measured contact impedances are compatible with predicted

values based on estimates of likely sensor capacitance, a separation of <1.5 mm between sensor foil and rock surface, and a dielectric medium comprising acetate, air, and water [*Tschofen*, 2014].

3.5.2. Apparent Resistivity Time Series

Multisensor CRI and ERT data were acquired regularly throughout the experiments over multiple freeze-thaw cycles. We illustrate the characteristics of apparent resistivity time series for both methodologies. A subset of the data spanning freeze-thaw cycles 4 to 9 (days 210 to 325 after the start of the experiments) is examined below.

3.5.2.1. Tuffeau (block 3): Active Layer Underlain by Permafrost

Figure 13a shows apparent resistivities estimated on block 3 (tuffeau) by a single four-sensor configuration (current dipoles C1 and C2 and potential dipoles P1 and P2) of CRI and ERT arrays, respectively. The apparent resistivities are plotted alongside the distribution of rock temperature (section 3.1) and surface heave/settlement observed on the block top (section 3.3). The sensor positions for this measurement are indicated as red (current) and green (potential) markers on the inset diagram showing the block outline. They were chosen such that all four sensors were located on the lower half of the tuffeau block, i.e., within the permafrost layer. The white dashed lines indicate the electrode positions relative to the rock temperature distribution.

Both CRI and ERT apparent resistivities tracked the rock temperature variations very clearly, with transitions between frozen and thawed conditions causing bulk resistivities to vary by a factor of at least ~4 relative to maximum values, in broadly repeatable patterns. CRI and ERT apparent resistivity estimates differed by a factor of ~2, with CRI consistently producing higher estimates. During freezing cycles, when the entire block was frozen, both techniques reached stable plateau values of maximum resistivities (CRI: ~10 kΩm; ERT: ~5 kΩm). During thawing periods, resistivity values gradually dropped in line with rising temperature and increase in liquid water content to eventually reach minimum levels (CRI: ~2.5 kΩm; ERT: ~1.5 kΩm). At this point in the experiment, both sets of geoelectrical data exhibited relatively low levels of noise. The total heave observed during freeze-thaw cycles 4 to 9 amounted to >3 mm, but no effect on the electrical data due to the uplift is immediately apparent from the time series associated with a single four-electrode combination. Such effects are more likely to become apparent during tomographic reconstruction of data from multiple electrode combinations.

3.5.2.2. Wetterstein (Block 6): Seasonal Frost

Figure 13b shows the same type of plot for a single four-sensor configuration of CRI and ERT arrays on block 6 (Wetterstein). Once again, both CRI and ERT apparent resistivities tracked the rock temperature variations closely, but average resistivities of the Wetterstein limestone were higher, in line with expectations. During freezing periods both techniques reached maximum resistivities of >150 kΩm (CRI) and ~70 kΩm (ERT), although more stable plateau values were observed with CRI. Compared with the tuffeau data, ERT measurements on Wetterstein exhibited substantial reciprocal errors (often >20%) and ERT struggled to determine a stable maximum resistivity of the frozen rock mass. During thawing periods, resistivity values gradually dropped, as with the tuffeau, and both techniques reached well-defined minimum levels (CRI: ~15 kΩm; ERT: ~7 kΩm). Transitions between frozen and thawed conditions therefore caused bulk resistivities to vary by a factor of at least ~10 relative to maximum values. Total observed heave was <1 mm, and again, no impact on the electrical data is apparent.

3.6. Microseismic Events

The calibrated triggering of more than 1000 microseismic events coincided with either low temperatures or strong changes in thermal forcing (i.e., conditions favoring ice segregation), while warm conditions from days 15 to 26 did not trigger seismic events (Figure 14). Frequent triggering (>40 events per day) often coincided with strong delta heave (days 3, 7, 9, 27, 49…), where the highest trigger frequencies corresponded to freezing and thawing days (12–13, 26–27, and 48–49).

4. Discussion

4.1. Weathering

The physical properties of the four tuffeau blocks changed during the experiments, as macrocracks developed by frost weathering. Macrocracking is attributed to ice segregation within the tuffeau blocks, as observed in previous experiments on this rock type [*Murton et al.*, 2001, 2006]. As expected, macrocracks
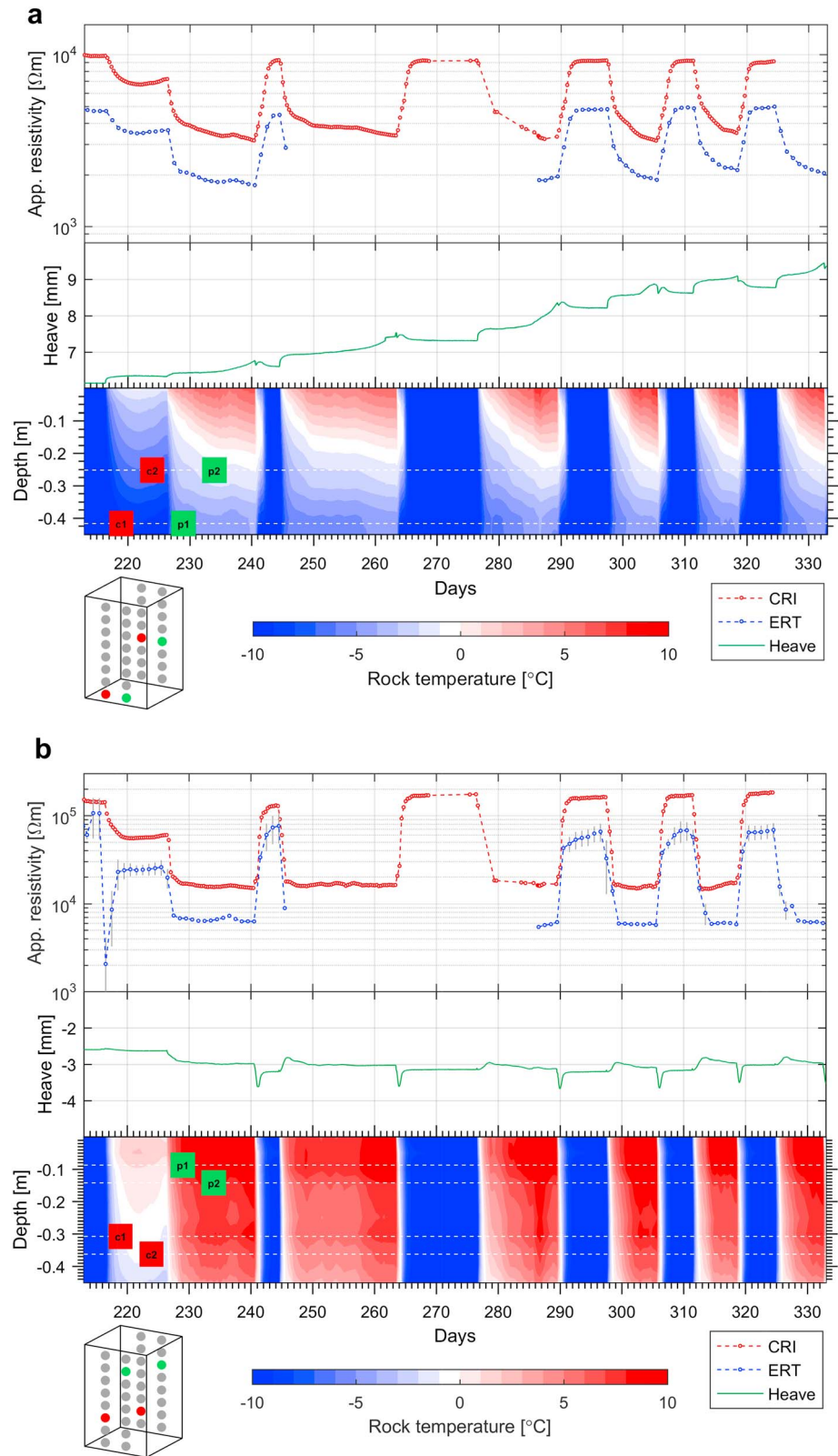
Figure 13. Example time series of geoelectrical data (CRI and ERT apparent resistivities) and heave, plotted alongside vertical rock temperature distribution during freeze-thaw cycles 4 to 9 (days 220 to 330). (a) Block 3 (tuffeau); (b) block 6 (Wetterstein). Reciprocal error for ERT shown as error bars. The electrode positions are shown on the inset diagram containing the block outline.
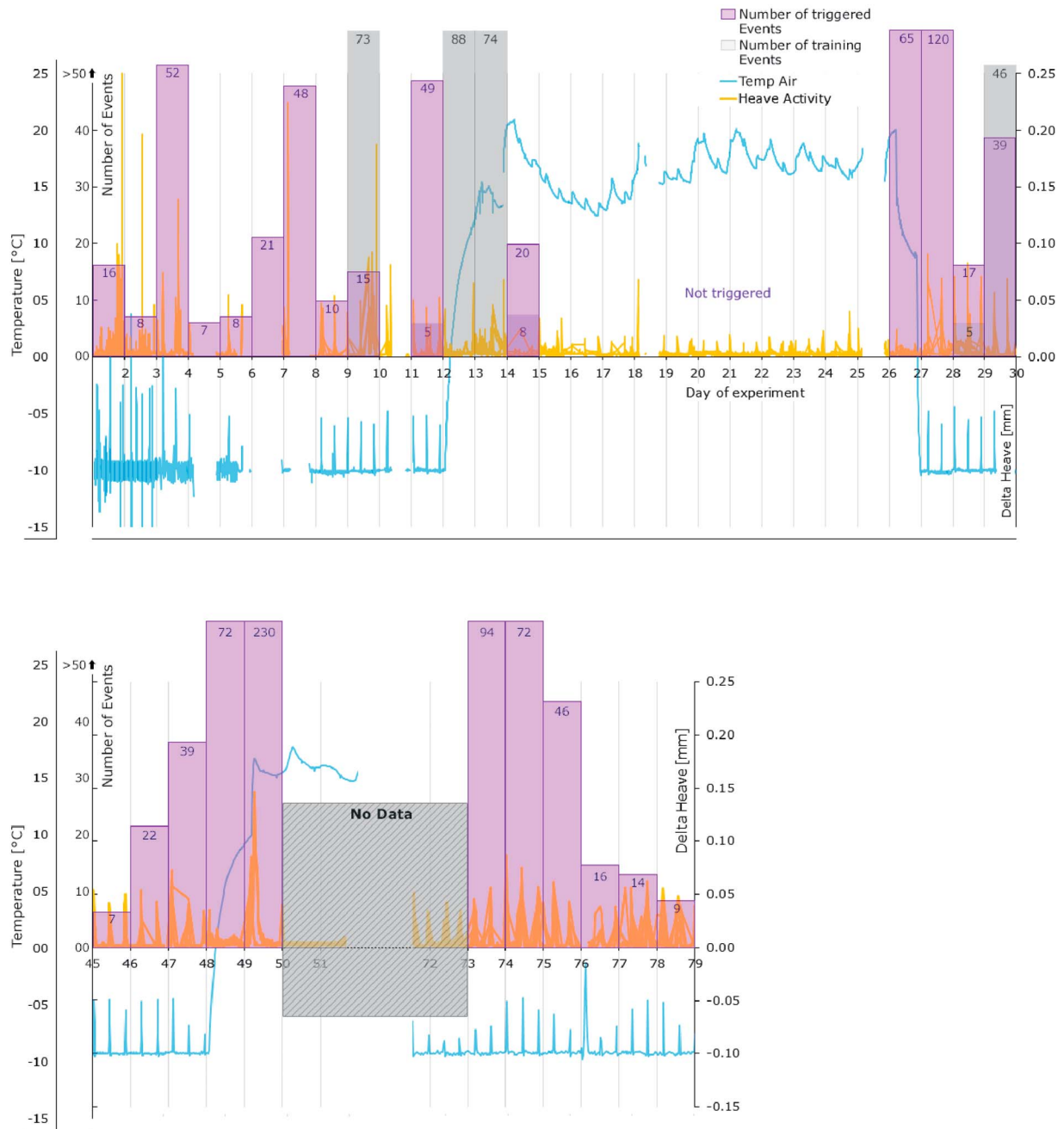
Figure 14. Number of triggered microseismic events coincident to air temperature regime and heave.

in the permafrost experiment concentrated in the upper part of the permafrost and the lower part of the active layer in tuffeau blocks 1 and 3, subject to bidirectional freezing. This led to a buildup of segregated ice in the near-surface permafrost and substantial heave of the block surface, interrupted episodically by melt of some segregated ice, and resultant settlement during particularly warm conditions.

In addition to ice segregation, corrosion of some TDR rods in tuffeau block 4 suggests that frost weathering was accompanied by chemical weathering. The type of chemical weathering is not known, but one possibility is oxidation of pyrite and/or destabilisation of glauconite within the tuffeau adjacent to the rods, as reported in weathering of tuffeau and the formation of the mineral jarosite in the walls of the thirteenth century abbey at Fontevrault, Maine-et-Loire, France [*Bauer and Velde*, 1997]. We speculate that the potent combination of

frost and chemical weathering may also account for the remarkable abundance and pervasive nature of macrocracks that formed in block 4 (Figures 9d and 10c) and the high-magnitude heave recorded (Figure 8). The orange brown discoloration indicates oxidation associated with chemical weathering of iron-bearing minerals. The highly corroded state of some TDR rods extracted from block 4 is consistent with localized formation of acid (e.g., sulphuric) during some stages of weathering.

4.2. Geoelectrical Monitoring

Our geoelectrical results highlight the additional challenge of applying conventional geoelectrical methodology to monitoring of permafrost-affected rocks, when compared to monitoring of permafrost dynamics in soils or unconsolidated sediments. Irrespective of the ambient temperatures and seasonal regime, the observed ERT contact impedances on our rock samples were at least 1–2 orders of magnitude higher than typical values observed with ERT monitoring arrays installed in soft soils or sediments [*Doetsch et al.*, 2015; *Tomaškovičová et al.*, 2016]. As shown in section 3.5.1, contact impedances observed on low-porosity, high-strength limestone are higher still (by factors of 20–50) compared with those achievable on high-porosity, low-strength chalk. This imposes even tighter restrictions on the viability of permafrost monitoring with ERT on rock walls or bedrock exposures, compared with those on lowland postglacial sediments, for example, as reported by *Tomaškovičová et al.* [2016]. By contrast, typical contact impedances achieved with CRI are demonstrably less affected by the seasonal changes in temperature, the aggregate state of the pore water (liquid or frozen), and the presence of low-porosity rock with high matrix resistivities. This is because CRI contact impedances are more likely to be dominated by the reactive component of the impedance associated with the capacitive coupling, as opposed to the (ohmic) resistive component associated with quasi-static current flow in the rock matrix [*Kuras et al.*, 2006]. Provided that the mechanical coupling of the capacitive sensor with the rock surface can be sufficiently well controlled, CRI therefore offers an opportunity to extend the benefits of geoelectrical monitoring methodology to soft/hard rock environments.

The time series of apparent resistivity (section 3.5.2) illustrate the performance of both ERT and CRI during the freeze-thaw experiments and their response to the changing environmental conditions. It is evident that both techniques are directly sensitive to the changes in rock temperature and associated variations in liquid water content, which controls ionic current flow. Essentially, both ERT and CRI make an equivalent measurement of (quasi-)DC electrical properties within the limitations of the experimental constraints, the differences in the physics of each measurement, and the differences in sensor geometry and location. The differences in sensor geometry and location, combined with the fact that apparent resistivities vary with measurement geometry, tend to make quantitative analysis and direct quantitative comparison between ERT and CRI apparent resistivities challenging and may account for much of the observed constant offset between both time series. Furthermore, limitations in the validity of the quasi-static approximation assumed for simple CRI data processing are known and can be quantitatively assessed by numerical simulation [*Uhlemann and Kuras*, 2014]. For small sensor separations, the point pole assumption starts to deteriorate, which can adversely affect CRI measurements derived from sensors placed in close proximity to each other. However, for the present configuration this effect is thought to be tolerable. The minimum normalized sensor separation l_r of the CRI sensors in the present experiment equals 1.1, which suggests maximum errors relative to the ideal point-pole solution on the order of ~10% [*Uhlemann and Kuras*, 2014]. Inverse modeling of ERT and CRI data yields spatial distributions of bulk resistivity, which will ultimately represent the yardstick for quantitative comparison between both techniques.

4.3. Microseismic Monitoring

After applying the four prefiltering criteria (section 2.4.3), we applied additional filtering criteria to detect and cluster relevant microcracking events out of the more than 1000 events reported in Figure 14. These criteria derive from previously published examples of best practice [*West et al.*, 2010; *Hammer et al.*, 2013, 2015] and highlight frequency and waveform as the criteria most indicative of microcracking in rock and ice masses. *Spillmann et al.* [2007] described brief seismic microcracking events up to 200 Hz, and *Senfaute et al.* [2009] classified signals, prior to rockfall, with the highest frequencies of 100–1000 Hz as crack initiation and fracture opening, whereas a decrease in the highest frequencies marked the extension and coalescence of existing microcracks. *Eberhardt et al.* [2004] estimated that frequencies of 100–500 Hz indicated brittle-fracture-induced seismicity. Lower frequencies, between 8 and 100 Hz, were reported for ice cracking [*O'Neel et al.*, 2007; *Neave and Savage*, 1970; *West et al.*, 2010]. These best practice examples also reported distinctive
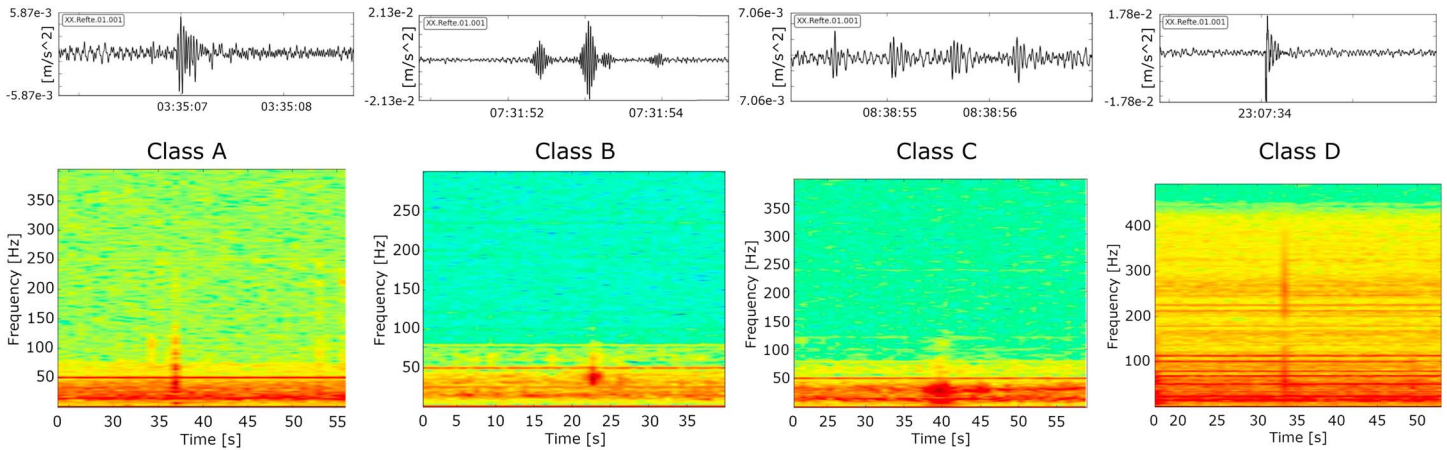
Figure 15. Frequency of Class A, B, C, and D microseismic events. The plots show seismic acceleration versus time and the relevant frequency during typical Class A–D events. Characteristics relevant for the clustering of the events are given in the text.

waveforms and durations [*West et al.*, 2010] for crack initiation, crack coalescence, and shearing, which we applied for our interpretation.

We grouped 42% of the ≥1000 triggered microseismic events in four event classes (Figure 15), based on checking waveform characteristics and event frequency automatically detected by the STA/LTA trigger, as performed in similar microseismicity analysis [*West et al.*, 2010; *Hammer et al.*, 2013, 2015]. Event class A shows an irregular, steep onset signal with a duration of 0.5–1.0 s and a frequency band up to 250 Hz. Event class B signal displays several wave patterns with an emergent onset, a duration exceeding 1.5 s and frequencies of 40–80 Hz. Event class C refers to signals with a sequence of instant waveforms, a duration greater than 2.0 s (whole signal), and frequencies below 50 Hz. Event class D consists of single-event signals with a steep onset, a duration shorter than 0.5 s, and frequency bands up to >250 Hz.

Class A to D microseismic events can be hypothetically referred to certain mechanisms based on onset characteristics, frequency, and the distribution of events relative to heave (Figure 16). Class D only occurs preheave and during heave and compares well to events characterized as shearing and/or opening of fracture prior to final failure by *Senfaute et al.* [2009]. Class A could be interpreted as crack initiation or the
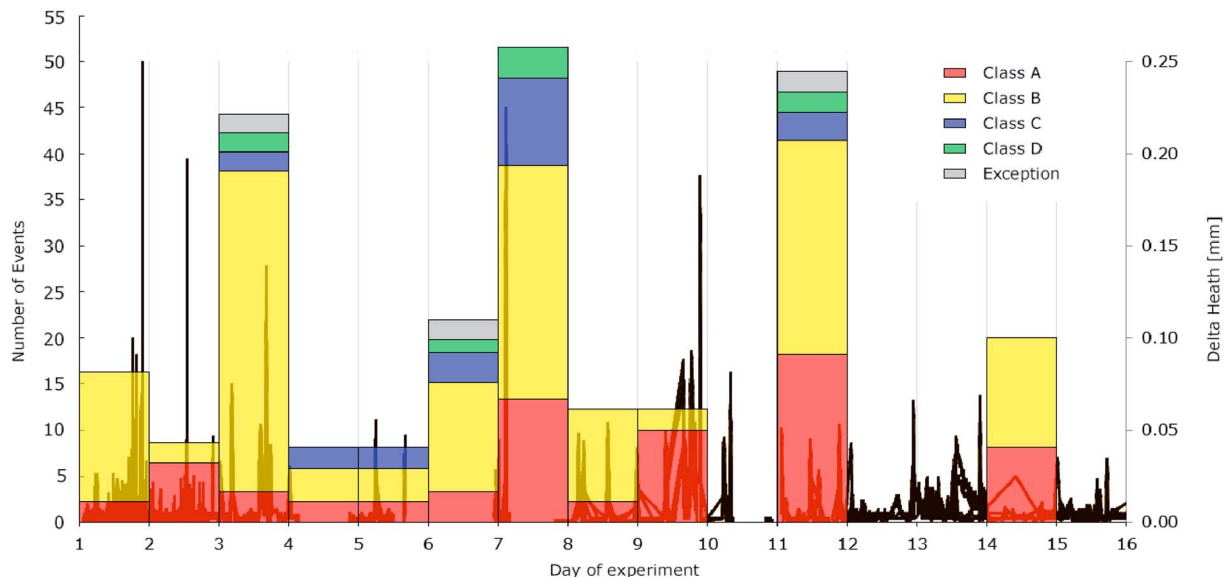

Figure 16. Number of class A to D microseismic events during days 1 to 14 of the experiment.

beginning of crack coalescence [*Eberhardt et al.*, 1999; *Senfaute et al.*, 2009]. In that way, classes B and C correspond best to multistage crack coalescence organized by repeated small connecting fractures and rock bridge yielding.

5. Conclusions

We have successfully integrated geophysical monitoring with controlled laboratory freeze-thaw experiments that simulated an active layer in rock above permafrost and seasonally frozen rock in a nonpermafrost environment. The experiments monitored temperature, volumetric unfrozen water content, and heave in four blocks of soft, initially intact chalk (tuffeau) and in two blocks of hard, initially fractured (Wetterstein) limestone. The volumetric unfrozen water content in two blocks of tuffeau varied between about $0.1\,m^3\,m^{-3}$ during monitored freezing periods and about 0.2 to $0.3\,m^3\,m^{-3}$ in the active layer of block 1 and throughout block 4 during thawing periods, peaking at 0.41 and $0.45\,m^3\,m^{-3}$ during early stages of thaw. Two blocks of tuffeau in the permafrost experiment developed fractures filled with segregated ice that were concentrated in the upper part of the permafrost and the lower part of the active layer, whereas two blocks of tuffeau in the seasonal frost experiment developed fractures almost to the bottom of the blocks. The fractures formed by ice segregation, although chemical weathering, may have been a contributory factor in one seasonally frozen block whose metal water content probes became strongly corroded.

Our novel CRI monitoring system has been effective at observing the geoelectrical signatures associated with freezing and thawing of a soft and a hard type of limestone over multiple freeze-thaw cycles, and in the presence or absence of artificial permafrost. Of particular importance is the demonstrated proof of concept that the CRI method is sensitive to the freezing and thawing of rock whose internal structure is changing progressively with the development of a fracture network. Our results show that CRI offers a viable route for nongalvanic long-term geoelectrical monitoring in the cryosphere and yields information equivalent to that obtainable with conventional ERT methodology. Multisensor CRI data acquisition has been demonstrated, and observations are compatible with model-based predictions, suggesting that CRI-derived apparent resistivities at the laboratory scale are suitable for tomographic reconstruction. In contrast to ERT, contact impedances achieved with CRI are less affected by the seasonal changes in temperature, the aggregate state of the pore water, and the presence of low-porosity rock with high matrix resistivities. This suggests that the CRI method holds good promise to its application to field conditions, where fractured bedrock is typical in mountain rockwalls.

More than 1000 microseismic events were detected during freeze-thaw cycles and grouped into four classes according to frequency and waveform. The classes are hypothesized to indicate shearing and/or fracture opening prior to final failure, crack initiation or the beginning of crack coalescence, and multistage crack coalescence. Monitoring of microseismic events holds promise for detecting crack initiation or coalescence during freezing and thawing of rock.

References

Bauer, A., and B. Velde (1997), Jarosite formation in weathered siliceous chalk in Fontevrault abbey, Loire Valley, France, *Mineral. Mag.*, *61*, 705–711, doi:10.1180/minmag.1997.061.408.10.

Doetsch, J., T. Ingeman-Nielsen, A. V. Christiansen, G. Fiandaca, E. Auken, and B. Elberling (2015), Direct current (DC) resistivity and induced polarization (IP) monitoring of active layer dynamics at high temporal resolution, *Cold Reg. Sci. Technol.*, *119*, 16–28, doi:10.1016/j.coldregions.2015.07.002.

Eberhardt, E., D. Stead, and B. Stimpson (1999), Quantifying progressive pre-peak brittle fracture damage in rock during uniaxial compression, *Int. J. Rock Mech. Min.*, *36*, 361–380, doi:10.1016/s0148-9062(99)00019-4.

Eberhardt, E., T. Spillmann, H. Maurer, H. Willenberg, S. Loew, and D. Stead (2004), The Randa Rockslide Laboratory: Establishing brittle and ductile instability mechanisms using numerical modelling and microseismicity, in *9th International Symposium of Landslides*, edited by W. A. Lacerda et al., pp. 481–487, A. A. Balkema, Leiden, Netherlands.

Hammer, C., M. Ohrnberger, and D. Faeh (2013), Classifying seismic waveforms from scratch: A case study in the alpine environment, *Geophys. J. Int.*, *192*, 425–439, doi:10.1093/gji/ggs036.

Hammer, C., M. Ohrnberger, and V. Schlindwein (2015), Pattern of cryospheric seismic events observed at Ekstrom Ice Shelf, Antarctica, *Geophys. Res. Lett.*, *42*, 3936–3943, doi:10.1002/2015GL064029.

Harris, C., et al. (2009), Permafrost and climate in Europe: Monitoring and modelling thermal, geomorphological and geotechnical responses, *Earth Sci. Rev.*, *92*(3–4), 117–171, doi:10.1016/j.earscirev.2008.12.002.

Hokett, S. L., J. B. Chapman, and C. E. Russell (1992), Potential use of time domain reflectometry for measuring water content in rock, *J. Hydrol.*, *138*(1), 89–96, doi:10.1016/0022-1694(92)90157-Q.

Ingeman-Nielsen, T., S. Tomaškovičová, and T. Dahlin (2016), Effect of electrode shape on grounding resistances. Part 1: The focus-one protocol, *Geophysics*, *81*(1), WA159–WA167, doi:10.1190/geo2015-0484.1.

Krautblatter, M. (2009), Detection and quantification of permafrost change in alpine rock walls and implications for rock instability, PhD thesis, Univ. of Bonn, Bonn, Germany. [Available at http://hss.ulb.uni-bonn.de/2009/1838/1838-engl.htm.]

Krautblatter, M., and C. Hauck (2007), Electrical resistivity tomography monitoring of permafrost in solid rock walls, *J. Geophys. Res.*, *112*, F02S20, doi:10.1029/2006JF000546.

Krautblatter, M., S. Verleysdonk, A. Flores-Orozco, and A. Kemna (2010), Temperature-calibrated imaging of seasonal changes in permafrost rock walls by quantitative electrical resistivity tomography (Zugspitze, German/Austrian Alps), *J. Geophys. Res.*, *115*, F02003, doi:10.1029/2008JF001209.

Kuras, O., D. Beamish, P. I. Meldrum, and R. D. Ogilvy (2006), Fundamentals of the capacitive resistivity technique, *Geophysics*, *71*(3), G135–G152, doi:10.1190/1.2194892.

Loke, M. H., J. E. Chambers, D. F. Rucker, O. Kuras, and P. B. Wilkinson (2013), Recent developments in the direct-current geoelectrical imaging method, *J. Appl. Geophys.*, *95*, 135–156, doi:10.1016/j.jappgeo.2013.02.017.

Mackay, J. R. (1998), Pingo growth and collapse, Tuktoyaktuk Peninsula area, western Arctic coast, Canada: A long-term study, *Géogr. Phys. Quat.*, *52*, 271–323, doi:10.7202/004847ar.

Murton, J. B., J. P. Coutard, J. P. Lautridou, J. C. Ozouf, D. A. Robinson, R. B. G. Williams, G. Guillemet, and P. Simmons (2000), Experimental design for a pilot study on bedrock weathering near the permafrost table, *Earth Surf. Processes Landforms*, *25*(12), 1281–1294, doi:10.1002/1096-9837(200011)25:12<1281::AID-ESP137>3.0.CO;2-U.

Murton, J. B., J. P. Coutard, J. P. Lautridou, J. C. Ozouf, D. A. Robinson, and R. B. G. Williams (2001), Physical modelling of bedrock brecciation by ice segregation in permafrost, *Permafrost Periglac. Processes*, *12*(3), 255–266, doi:10.1002/ppp.390.

Murton, J. B., R. Peterson, and J. C. Ozouf (2006), Bedrock fracture by ice segregation in cold regions, *Science*, *314*(5802), 1127–1129, doi:10.1126/science.1132127.

Neave, K. G., and J. C. Savage (1970), Icequakes on the Athabasca Glacier, *J. Geophys. Res.*, *75*, 1351–1362, doi:10.1029/JB075i008p01351.

O'Neel, S., H. P. Marshall, D. E. McNamara, and W. T. Pfeffer (2007), Seismic detection and analysis of icequakes at Columbia Glacier, Alaska, *J. Geophys. Res.*, *112*, F03S23, doi:10.1029/2006JF000595.

Sass, O. (2004), Rock moisture fluctuations during freeze-thaw cycles—Preliminary results derived from electrical resistivity measurements, *Polar Geogr.*, *28*(1), 13–31, doi:10.1080/789610157.

Sass, O. (2005), Rock moisture measurements: Techniques, results, and implications for weathering, *Earth Surf. Processes Landforms*, *30*, 359–374, doi:10.1002/esp.1214.

Senfaute, G., A. Duperret, and J. A. Lawrence (2009), Micro-seismic precursory cracks prior to rock-fall on coastal chalk cliffs: A case study at Mesnil-Val, Normandie, NW France, *Nat. Hazards Earth Syst. Sci.*, *9*, 1625–1641, doi:10.5194/nhess-9-1625-2009.

Spillmann, T., H. Maurer, A. G. Green, B. Heincke, H. Willenberg, and S. Husen (2007), Microseismic investigation of an unstable mountain slope in the Swiss Alps, *J. Geophys. Res.*, *112*, B07301, doi:10.1029/2006JB004723.

Tomaškovičová, S., T. Ingeman-Nielsen, A. V. Christiansen, I. Brandt, T. Dahlin, and B. Elberling (2016), Effect of electrode shape on grounding resistances. Part 2: Experimental results and cryospheric monitoring, *Geophysics*, *81*(1), WA169–WA182, doi:10.1190/geo2015-0148.1.

Topp, G. C., J. L. Davis, and A. P. Annan (1980), Electromagnetic determination of soil-water content—Measurements in coaxial transmission-lines, *Water Resour. Res.*, *16*, 574–582, doi:10.1029/WR016i003p00574.

Tschofen, D. (2014), Geoelectrical monitoring of rock permafrost in the laboratory, MSc thesis, ETH Zurich, Zurich, Switzerland.

Uhlemann, S., and O. Kuras (2014), Numerical simulations of capacitive resistivity imaging (CRI) measurements, *Near Surf. Geophys.*, *12*(4), 523–537, doi:10.3997/1873-0604.2014008.

Vaezi, Y., and M. Van der Baan (2014), Analysis of instrument self-noise and microseismic event detection using power spectral density estimates, *Geophys. J. Int.*, *197*, 1076–1089, doi:10.1093/gji/ggu036.

West, M. E., C. F. Larsen, M. Truffer, S. O'Neel, and L. LeBlanc (2010), Glacier microseismicity, *Geology*, *38*, 319–322, doi:10.1130/g30606.1.

Zonge, K. L., and L. J. Hughes (1986), Effect of electrode contact resistance on electric field measurements, *Geophysics*, *51*(2), 463.